The Astrophysical Journal, 994:44 (20pp), 2025 November 20 https://doi.org/10.3847/1538-4357/ae0b59

Investigating Non-LTE Abundances of Neodymium in Metal-poor FGK Stars

John D. Dixon[1,2,3], Rana Ezzeddine[2], Yangyang Li[2], Thibault Merle[4,5], Manuel Bautista[6], and Yanjun Guo[7]
[1] Department of Physics and Astronomy, Texas A&M University, College Station, TX 77843, USA; johndixon@tamu.edu
[2] Department of Astronomy, University of Florida, Gainesville, FL 32601, USA
[3] Mitchell Institute for Fundamental Physics and Astronomy and Department of Physics and Astronomy, Texas A&M University, College Station, TX 77843, USA
[4] Institut d'Astronomie et d'Astrophysique and Brussels Laboratory of the Universe (BLU-ULB), Université Libre de Bruxelles, CP 226, 1050 Brussels, Belgium
[5] Royal Observatory of Belgium, Avenue Circulaire 3, 1180 Brussels, Belgium
[6] United States Department of Energy, Washington, DC 20585, USA
[7] Yunnan Observatories, Chinese Academy of Sciences (CAS), Kunming 650216, Yunnan, People's Republic of China
Received 2025 May 7; revised 2025 September 23; accepted 2025 September 23; published 2025 November 13

Abstract

The dominant site(s) of the *r*-process are a subject of current debate. Ejecta from *r*-process-enrichment events like kilonovae are difficult to directly measure, so we must instead probe abundances in metal-poor stars to constrain *r*-process models. This requires state-of-the-art non-LTE (NLTE) modeling, as LTE is a poor approximation for the low-opacity atmospheres of metal-poor giants. Neodymium (Nd) is a prominent *r*-process element detected in both near-infrared kilonova spectra and the spectra of metal-poor stars, so precise Nd stellar abundances are particularly needed to model kilonovae and constrain *r*-process sites. We thus constructed an Nd I/Nd II model atom to compute NLTE abundances in FGK metal-poor stars. We obtain $A(\mathrm{Nd})_{\odot} = 1.44 \pm 0.05$, in agreement with the meteoritic value, when calibrating the model atom with a Drawin hydrogen collision factor of $S_{\mathrm{H}} = 0.1$. For a sample of metal-poor *r*-process-enhanced stars with observed optical and near-infrared Nd II lines, we find NLTE Nd corrections in the range −0.3 to 0.3 dex. Optical and UV lines have positive NLTE corrections, whereas *H*-band lines have negative corrections. Additionally, we compute a large grid of NLTE corrections for 122 Nd II spectral lines ranging from the UV to the *H* band, for stellar parameters of typical metal-poor FGK dwarfs and giants with $-3 \leqslant [\mathrm{Fe/H}] \leqslant -1$ and $-2 \leqslant A(\mathrm{Nd}) \leqslant 2$. Within this grid, we find NLTE corrections ranging from −0.3 to +0.5 dex. Deviations from LTE are found to be strongest for blue lines with low excitation potentials in the most metal-poor giants.

Unified Astronomy Thesaurus concepts: F stars (519); Stellar abundances (1577); G stars (558); K stars (878); Stellar atmospheres (1584); Chemical abundances (224); Atomic data (2216); Galactic archaeology (2178)

1. Introduction

The origins of heavy elements are a key focus of stellar archaeology, and approximately half of all isotopes heavier than iron are typically created via the rapid neutron-capture process (*r*-process), which requires extreme neutron densities above $\sim 10^{22}$ cm^{-3} (A. Frebel 2018). The sites of the *r*-process are still highly debated, with collapsars (D. M. Siegel et al. 2019), exotic supernovae (N. Nishimura et al. 2017), and neutron star mergers (NSMs; D. Watson et al. 2019) among the possible candidates. The detection of GW170817 led to the discovery of heavy element ejecta from a kilonova explosion via radioactive decay as imprinted on its spectra, prompting more research into the rates at which NSMs form the *r*-process abundances observed in stars today. As we are unable to measure abundances from direct observations of kilonovae due to heavily blurred spectral lines from extreme Doppler shifts, models of *r*-process events can be otherwise constrained using traces of *r*-process elements found in second-generation metal-poor ($[\mathrm{Fe/H}] < -1.0$) stars. These stars are pristine and are believed to have formed from the ejecta of one or a few *r*-process events, preserving clear signatures of *r*-process elements in their atmospheres after birth (A. Frebel 2010, 2018).

Determining accurate ejecta of *r*-process events as preserved in metal-poor stars requires high-precision *r*-process elemental abundance calculations. Due to recent efforts led by large spectroscopic surveys including the *R*-Process Alliance (T. T. Hansen et al. 2018; C. M. Sakari et al. 2018; R. Ezzeddine et al. 2020; E. M. Holmbeck et al. 2020; A. Bandyopadhyay et al. 2024), LAMOST (T.-Y. Chen et al. 2021), GALAH (G. M. De Silva et al. 2015; S. L. Martell et al. 2017; S. Buder et al. 2018, 2021, 2025), as well as others, the number of discovered *r*-process-enhanced stars has vastly increased in recent years. The bulk of abundance analyses of these stars have been done under the atmospheric assumption of local thermodynamic equilibrium (LTE). Spectral lines forming in metal-poor star atmospheres, however, can significantly deviate from LTE models, particularly due to a deficiency of metal electron donors in the stellar atmosphere. This leads to a larger temperature gradient that increases overionization, as well as lower atmospheric opacities that allow photons to carry nonlocal information during spectral line formation, causing systematic (and sometimes significant) under- or overestimation of abundances relative to LTE (L. Mashonkina et al. 2011; M. Bergemann 2014; R. Ezzeddine et al. 2017; K. Lind & A. M. Amarsi 2024). Non-LTE (NLTE) effects for spectral lines are relative to the elemental abundance, and heightened in stellar atmospheres with lower metal abundances. Therefore, to reliably calculate *r*-process abundances in metal-poor stars, we must account for NLTE modeling effects.

Neodymium (Nd, $Z = 60$) is a neutron-capture element produced by both the *s*-process and *r*-process in similar quantities (C. Arlandini et al. 1999), which limits its ability to act as a tracer for either process. However, according to recently generated synthetic spectra and NLTE models of kilonovae (K. Hotokezaka

et al. 2021; Q. Pognan et al. 2023), Nd is one of the dominant lanthanides detectable in the ejecta of a kilonova, and so accurate measurements of Nd in stars known to have *r*-process enhancement are still crucial for probing NSMs and constraining *r*-process models. Nd has been measured in both optical and near-infrared (NIR) stellar spectra (S. Hasselquist et al. 2016; M. Afşar et al. 2018) and it is very useful for detecting *r*-process-enrichment signatures of stars in the Galactic plane due to having several observable spectral lines in the NIR, which are less affected by dust extinction (J. V. Sales-Silva et al. 2024). Since only lines from the dominant species (Nd II) have been measured so far in FGK stars, the abundance analysis of Nd has typically assumed LTE. A. G. A. Abdelkawy et al. (2017) investigated NLTE abundances for Nd II lines in the Sun and found negligible average NLTE abundance corrections of ∼0.01 dex to the standard LTE abundance. Another study by L. Mashonkina et al. (2005) determined NLTE abundances for Nd II and Nd III lines in A-type stars, and found much larger corrections than the Sun of up to ∼1 dex, which intensified with increasing stellar effective temperature. They found that NLTE calculations were able to decrease the abundance difference between Nd II and Nd III lines observed in chemically peculiar Ap stars, significantly reducing the LTE ionization imbalance between first- and second-ionized species. Nevertheless, NLTE effects on Nd in FGK *r*-process-enhanced metal-poor stars have not been tested for either the optical or NIR wavelength ranges yet to our knowledge. Additionally, recent models show that NLTE effects may indeed be nonnegligible for ionized dominant species of other heavy neutron-capture elements like yttrium (N. Storm & M. Bergemann 2023), europium (Y. Guo et al. 2025), strontium, and barium (L. Mashonkina et al. 2023).

In this paper, we thus present a novel Nd I/Nd II model atom which we thoroughly test for NLTE abundance analysis in FGK-type stars, over a wide range of stellar parameters and [Nd/Fe] abundance ratios. Section 2 details the construction and calibration of this model atom, and in Section 3, we use our Nd model atom to analyze NLTE abundances in a sample of well-studied metal-poor stars and demonstrate the necessity of calculating NLTE corrections for a wide range of stellar parameters. Following this, we analyze a grid of such corrections for metal-poor FGK star parameters and discuss the physical implications of these calculations in Section 4.

2. The Model Atom

In this section, we provide details on the construction, calibration, and testing of an Nd model atom to be used for NLTE abundance analysis of FGK stars.

2.1. Construction from Atomic Data

To calculate NLTE Nd abundances in stars, a model atom must first be assembled to account for as many transitions as possible, both radiatively and collisionally induced. Energy levels, electron configurations, and transition probabilities for this model were collected from existing literature and experimental atomic databases. To generate photoionization cross sections and collisional information for the model atom, we use the Python based code `FORMATO3` (T. Merle et al. 2011).[8] `FORMATO3` is an efficient and fast code that is useful for generating large model atoms that are compatible with the NLTE radiative transfer code `MULTI2.3` (M. Carlsson 1986, 1992), which we used in this work.

Spectral lines for Nd I and Nd II were extracted from the Vienna Atomic Line Database (VALD; W. F. Meggers et al. 1975; E. Biémont et al. 1999; F. Kupka et al. 1999; H. L. Xu et al. 2003, and references therein).[9] Energy levels from VALD were complemented by cross referencing with Nd I and Nd II energy levels obtained from the NIST Atomic Spectral Database (W. Martin et al. 1978; J. Blaise et al. 1984; D. A. Johnson & P. G. Nelson 2017).[10] We also implemented reliable $\log(gf)$ values from the open-source database Linemake (E. A. Den Hartog et al. 2003; I. U. Roederer et al. 2008; V. M. Placco et al. 2021)[11] whenever possible. Details of the energy levels and bound–bound transitions are presented in the Grotrian diagrams of Figure 1. In this figure, 114 optical transitions and eight NIR transitions are highlighted in red; these transitions are of particular interest for this study, as they have been previously observed in stellar spectra (sources for these observations are provided later in Section 3.2). The total numbers of levels, transitions, and collisions in the model atom are given in Table 1.

Our final constructed model atom contains 268 Nd I levels and 556 Nd II levels, and is closed by the ground state of Nd III. Additionally, a total of 1550 bound–bound transition lines were included from VALD, including 281 Nd I lines and 1269 Nd II lines. We also added eight NIR Nd II lines from S. Hasselquist et al. (2016) for analysis purposes.

For bound–free transitions, we used the classical approximation following Kramer's law (L. D. Travis & S. Matsushima 1968) to approximate the photoionization cross section as a function of frequency:

$$\sigma_{\nu}^{ic} = \sigma_{\nu 0}^{ic}\left(\frac{\nu}{\nu_0}\right)^{-3},$$

where ν is the photon frequency, and ν_0 is the minimum threshold frequency required to ionize the energy level i, whose photoionization cross section $\sigma_{\nu 0}^{ic}$ (in cm^{-2}) is given by

$$\sigma_{\nu 0}^{ic} = 7.91 \times 10^{-22}\frac{n}{Z^2}g_{\mathrm{rad}}^{ic},$$

where n is the principal quantum number of the electron configuration of the lower level i, Z is the atomic number of the element ($Z = 60$ for Nd), and g_{rad}^{ic} is the Gaunt factor, a corrective factor accounting for departure from classical physical models (R. Ezzeddine et al. 2016), which `FORMATO3` calculates using results from D. H. Menzel & C. L. Pekeris (1935), W. J. Karzas & R. Latter (1961), and C. Janicki (1990).

We also coupled all of our energy levels via inelastic electron and hydrogen collisional transitions. For electron collisional cross sections, the Seaton approximation was used to calculate both allowed transitions (M. J. Seaton 1962a) and forbidden transitions (M. J. Seaton 1962b). For inelastic hydrogen collisions, we used the Drawin approximation (H. W. Drawin 1968, 1969), multiplied by a scaling factor (S_{H}).

[8] https://github.com/thibaultmerle/formato3

[9] http://vald.astro.uu.se/∼vald/php/vald.php

[10] https://physics.nist.gov/PhysRefData/ASD/levels_form.html

[11] https://github.com/vmplacco/linemake

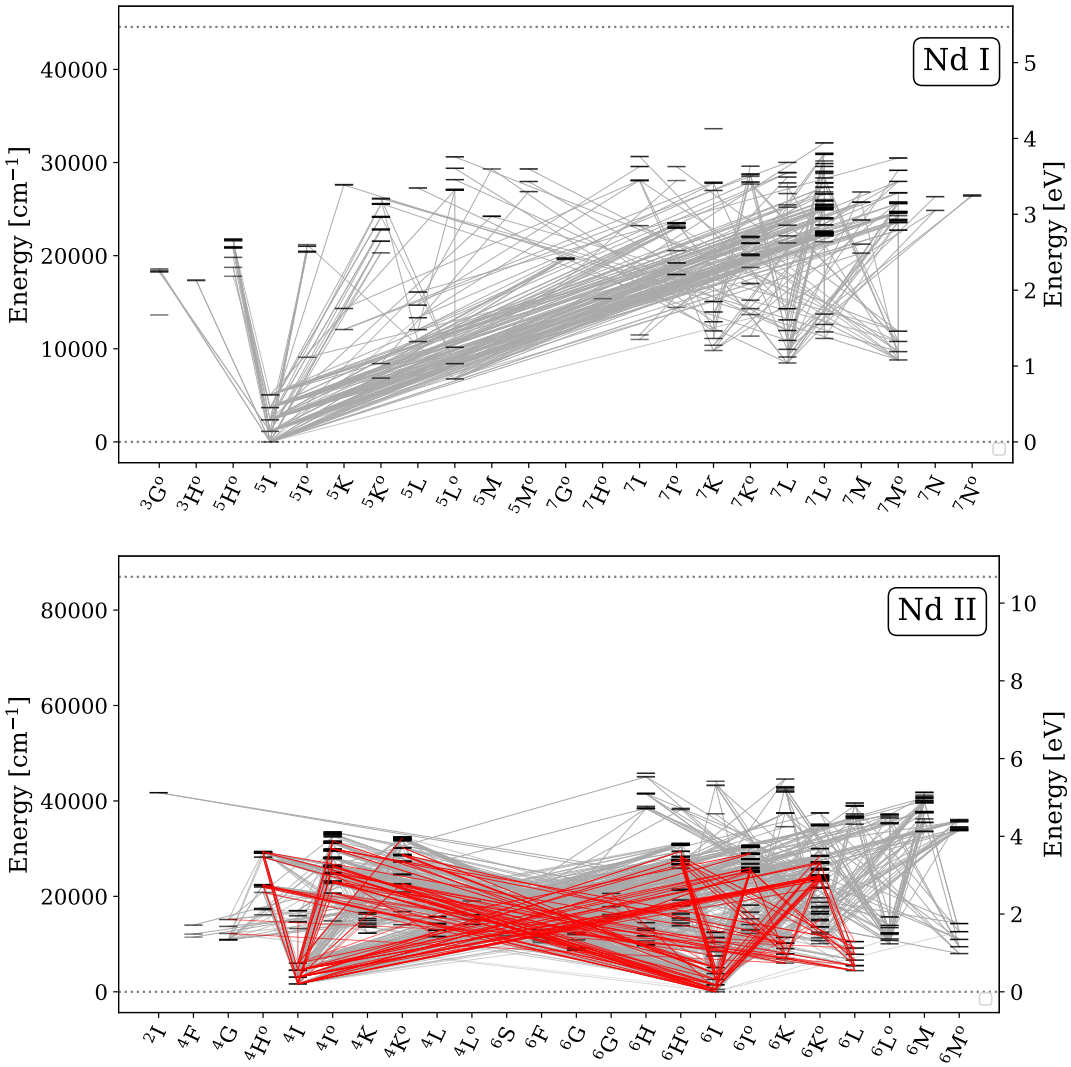

Figure 1. Grotrian diagrams of Nd I and Nd II displaying all energy levels and bound–bound transitions as generated by `FORMATO3`. Spectral line data were assembled from VALD, NIST, Linemake, and S. Hasselquist et al. (2016). Dotted lines indicate the ground state and ionization energy of each species, and 122 transitions of interest that have been previously observed in stellar spectra are highlighted in red.

Table 1
Makeup of the Nd Model Atom

	Nd I	Nd II	Nd III	Total
Levels	268	556	1	825
Bound–Bound Transitions	281	1277	⋯	1558
Bound–Free Transitions	268	556	⋯	824
Electron Bound–Bound Collisions	35,778	154,290	⋯	190,068
Electron Bound–Free Collisions	268	556	⋯	824
Hydrogen Bound–Bound Collisions	281	1277	⋯	1558
Hydrogen Bound–Free Collisions	268	556	⋯	824

References. T. Merle et al. (2011), S. Hasselquist et al. (2016), VALD.

2.2. Model Atmospheres and Radiative Transfer Codes

In this work, our analysis utilizes the NLTE radiative transfer code `MULTI2.3` to generate curves of growth (COGs) for abundance analysis and the computation of NLTE corrections detailed in Section 3.3. `MULTI2.3` is a widely used open-source radiative transfer code used to compute NLTE and LTE level populations and NLTE line profiles. `MULTI2.3` uses background opacities from the 1973 Uppsala package (B. Gustafsson et al. 2008 and references therein) to model the spectral continuum. As we are primarily concerned with FGK stars, we adopt the widely used 1D, LTE MARCS grid of model atmospheres (B. Gustafsson et al. 2008) for analysis, with spherical models for giant stars ($\log g \lesssim 3.0$) and plane-parallel models for dwarf stars ($\log g \gtrsim 3.0$). We adopt model atmospheres with the alpha-enhanced "standard" mixture of metals as defined in the MARCS documentation.[12] These models use the α-element abundances $[\alpha/\mathrm{Fe}] = 0.0$ for $[\mathrm{Fe/H}] \geqslant 0.00$, $[\alpha/\mathrm{Fe}] = +0.4$ for $[\mathrm{Fe/H}] \leqslant -1.00$, and $[\alpha/\mathrm{Fe}]$ scaling linearly between these two values for $-1.00 \leqslant [\mathrm{Fe/H}] \leqslant 0.00$. We interpolated MARCS model atmospheres for adopted stellar parameters (T_{eff}, $\log g$, [Fe/H], and ξ_t) using the routine `interpol_marcs.f`, created by T. Masseron.[13]

To generate the NLTE synthetic spectra, we used the NLTE-enabled spectral synthesis code `Turbospectrum` (TS-NLTE; B. Plez 2012; J. M. Gerber et al. 2023) as explained in

[12] https://marcs.astro.uu.se/docs.html
[13] https://marcs.astro.uu.se/software.html

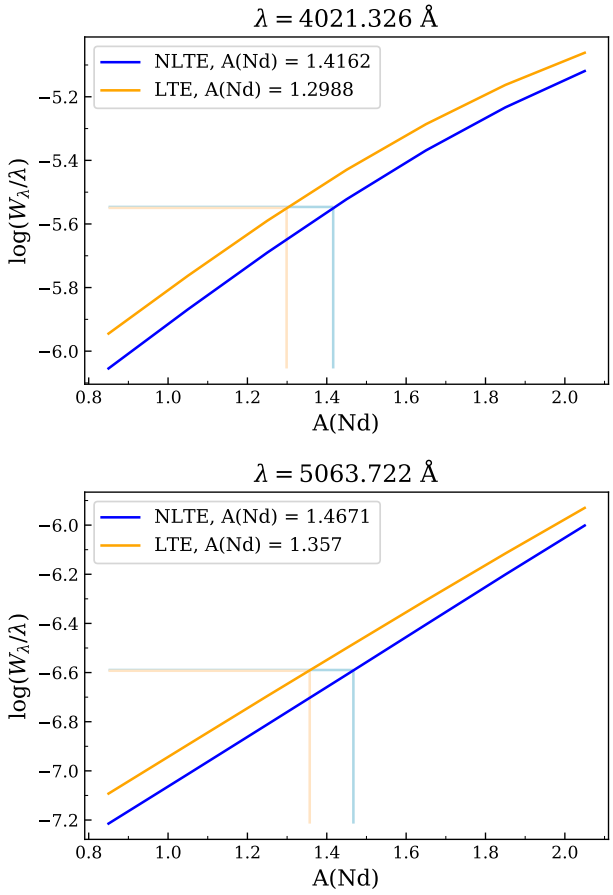

Figure 2. COGs for two Nd II lines generated with `MULTI2.3` using the solar MARCS model. Measured EWs from E. A. Den Hartog et al. (2003) were converted into A(Nd) values in both NLTE (dark blue) and LTE (light orange) by interpolating from a cubic best-fit curve.

Section 3.1. The code was updated with an NLTE correction grid centered around the star's parameters, generated by `MULTI2.3` using our new Nd I/Nd II model atom. We note that while we use TS-NLTE for comparison between synthetic and observed spectra as shown in Figure 5, we do not use it to fit or derive abundances.

2.3. Testing on the Sun and Calibrating S_H

With the Nd model atom generated as described above, we proceeded by deriving NLTE and LTE Nd abundances for the Sun. We determine the abundances of each Nd II line using a COG method based on the computed equivalent width (EW) for each input A(Nd) value. `MULTI2.3` computes departure coefficients, allowing for comparison between the NLTE and LTE abundances for each line.

For the solar-abundance analysis, we chose 25 optical Nd II lines (listed in Appendix Table A1) with EWs measured by E. A. Den Hartog et al. (2003) from a solar spectrum collected with the 1 m Fourier Transform Spectrometer at the National Solar Observatory. Figure 2 shows two example COGs computed for the two solar Nd II lines at 4021 Å and 5063 Å, respectively. The figure also shows the observed EW for each line and the abundance it corresponds to for both COGs; the horizontal distance between the two COGs gives the NLTE correction for a particular EW. The final solar Nd abundance was calculated by averaging the abundances derived from all 25 solar lines, to determine $A(\mathrm{Nd})_{\odot}$. Figure 3 shows average solar abundances derived for LTE and NLTE models employing different S_{H} factors ranging from 0.001 to 1.0, using both MARCS and the solar Holweger–Mueller (HM) model (H. Holweger & E. A. Mueller 1974). In addition, we generated similar box plots from 98 observed Nd II lines for HD 222925—a highly enhanced r-process benchmark star with a previously derived LTE Nd abundance from I. U. Roederer et al. (2018). For both stars, our derived abundances are higher with the NLTE models as compared to LTE. This is in line with predictions of NLTE abundances for dominant species in FGK-type atmospheres (M. Bergemann et al. 2012; K. Lind et al. 2012; R. Ezzeddine et al. 2017).

For the Sun, we derive an LTE Nd abundance of 1.335 ± 0.053 with a MARCS model atmosphere. Our derived NLTE values of $A(\mathrm{Nd})_{\odot}$ with MARCS models are 1.410 ± 0.056, 1.436 ± 0.050, 1.440 ± 0.048, and 1.441 ± 0.047 for $S_{\mathrm{H}} = 1.0$, 0.1, 0.01, and 0.001, respectively. These are in close agreement with the meteoritic value of 1.43 ± 0.03 (N. Grevesse et al. 2007). For HD 222925, we derive an LTE Nd abundance of 0.722 ± 0.057. Our derived NLTE abundances are 0.867 ± 0.061, 0.892 ± 0.058, 0.901 ± 0.070, and 0.902 ± 0.073 for $S_{\mathrm{H}} = 1.0$, 0.1, 0.01, and 0.001, respectively. We provide the LTE abundance from I. U. Roederer et al. (2018) to show the size of these error bars, but note that our values were computed using a different MARCS model atmosphere with rederived NLTE stellar parameters that are discussed further in Section 3.2. As both stars yield a small spread in average A(Nd) as a function of S_{H}, any abundance uncertainty arising from the choice of S_{H} is likely negligible compared to other sources of uncertainty. A full list of the line-by-line solar Nd abundances determined for each S_{H} value, as well as the average abundances, are given in the Appendix Table A1.

It is worth noting that our derived solar LTE abundance differs from the abundance reported in E. A. Den Hartog et al. (2003) by ~0.1 dex. This difference likely arises from the different model atmosphere and radiative transfer codes used in both studies: E. A. Den Hartog et al. (2003) used the empirical 1D HM model atmosphere (H. Holweger & E. A. Mueller 1974), while our analysis employs a theoretical MARCS solar 1D, LTE model. For the 25 common solar lines analyzed in this work, the mean and standard deviation of the reported abundances in E. A. Den Hartog et al. (2003) is $A(\mathrm{Nd}) = 1.44 \pm 0.04$. For comparison, we ran `MULTI2.3` with the HM model atmosphere, for which we derived $A(\mathrm{Nd}) = 1.40 \pm 0.05$ in LTE and $A(\mathrm{Nd}) = 1.48 \pm 0.05$ in NLTE for the same 25 lines. Both of these abundances agree with the value from E. A. Den Hartog et al. (2003) to within 1σ.

2.4. Testing Atom Completeness

We note that the highest experimental Nd II energy level from VALD and NIST is 45,801.380 cm^{-1}, which is significantly lower than the second ionization energy of Nd at 86,970 cm^{-1}. To test whether this large energy gap affects our NLTE results, we created three additional versions of the Nd model atom described in Section 2.1, henceforth referred to as atoms A, B, and C. These models supplement the 556 Nd I energy levels and 1277 Nd II lines from VALD and NIST with theoretically computed Nd II levels and lines from G. Gaigalas et al. (2019). For atom A, we added 251 theoretical levels and 162 new lines; atom B contains an additional 515 theoretical

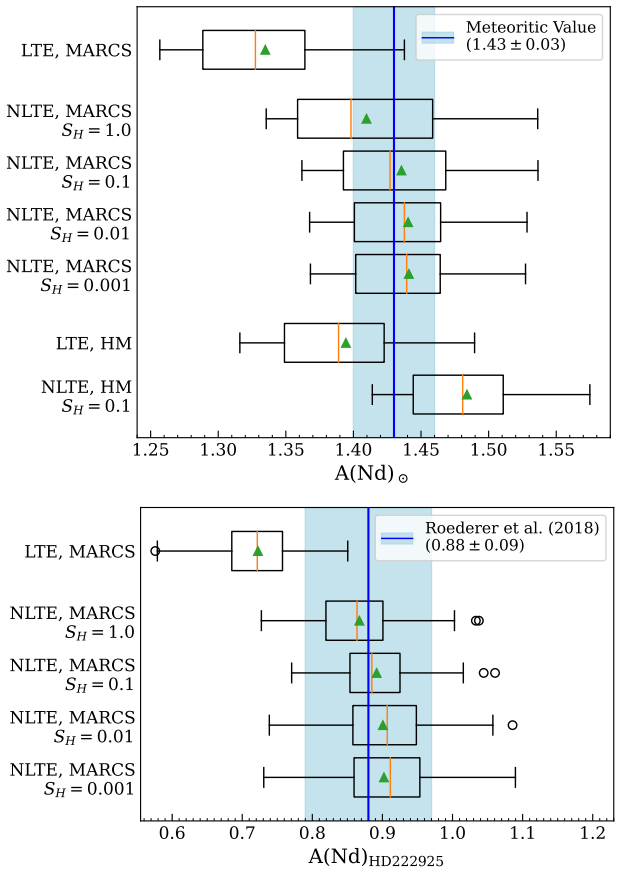

Figure 3. Nd II abundance calculations based on observed lines for the Sun (top) and HD 222925 (bottom) for LTE and NLTE models with different S_H factors, compared to published A(Nd) values (shown as blue shaded regions). Vertical axis labels indicate whether the HM model or a MARCS model atmosphere were used for the different S_H factors. Orange lines show the median of the line-by-line Nd abundances, while green triangles show the mean. The lower and upper boundaries of the boxes represent the first and third quartiles of the line-by-line abundances, respectively, with outliers shown as black circles.

levels and 2009 new lines; and atom C contains an additional 1055 theoretical levels and 7967 new lines. Grotrian diagrams of Nd II for these three model atoms are shown in Figure 4. The added theoretical levels have energies above 30,000 cm^{-1}, and all three subsets of levels were chosen to roughly preserve the relative density of levels as a function of energy. To construct atom A, we first arranged all theoretical levels above 30,000 cm^{-1} by energy and sampled 251 levels at evenly spaced indices. We then compiled a list of every theoretical bound–bound transition involving only these 251 levels, undersampling theoretical transitions as necessary in order to make computations tractable and avoid overloading `MULTI2.3`. We reviewed these transitions to ensure sufficient coupling between the experimental and theoretical levels, and then we added the theoretical levels and transitions to our compiled experimental data to create the final atom A. This same procedure was used to construct atoms B and C, with the only difference being the number of energy levels sampled, as shown in Table 2.

For each of these three model atoms, we rederived NLTE abundances for the 25 solar Nd II lines mentioned above, as well as for 98 Nd II lines from HD 222925—a highly enhanced r-process benchmark star with a previously derived LTE Nd abundance from I. U. Roederer et al. (2018). Table 2 shows the average and standard deviation of the derived $A(\mathrm{Nd})_{\mathrm{NLTE}} - A(\mathrm{Nd})_{\mathrm{LTE}}$ value (i.e., the NLTE correction, henceforth referred to as ΔA_{NLTE}) from spectral lines in both stars. The differences in NLTE corrections between different model atoms are negligible and the spread of the line-by-line NLTE corrections stays within a reasonable margin of error for abundance analysis, indicating that NLTE modeling effects do not change significantly with the addition of higher-energy theoretical levels and associated lines. Even in the case that the current data from VALD only accounts for ∼one-third of all Nd II levels and ∼one-sixth of all Nd II lines (atom C), the NLTE modeling effects for currently known lines in both the Sun and r-process-enhanced star HD 222925 are unaffected. Thus, going forward, we adopt the model atom constructed from experimental VALD and NIST data as our final atom for the rest of this study.

As another test of our NLTE model, we computed NLTE corrections for a small set of model atmospheres with typical A-type main-sequence parameters ($\log g = 4.0$, $[\mathrm{Fe/H}] = -1.50$, $\xi_t = 1.0$ km s^{-1}, and 7500 K $\leqslant T_{\mathrm{eff}} \leqslant$ 8000 K) with an Nd enhancement of $[\mathrm{Nd/H}] = 2.5$. These stellar parameters are outside the scope of our work, but the goal of this analysis was to compare ΔA_{NLTE} values from our model atom to those from L. Mashonkina et al. (2005), which were calculated with theoretical atomic data. For the Nd II lines at $\lambda = 4061$, 4706, and 5319 Å, our corrections are in agreement with L. Mashonkina et al. (2005) to within a typical margin of error for abundance analysis (±0.2 dex) and trend in the same direction

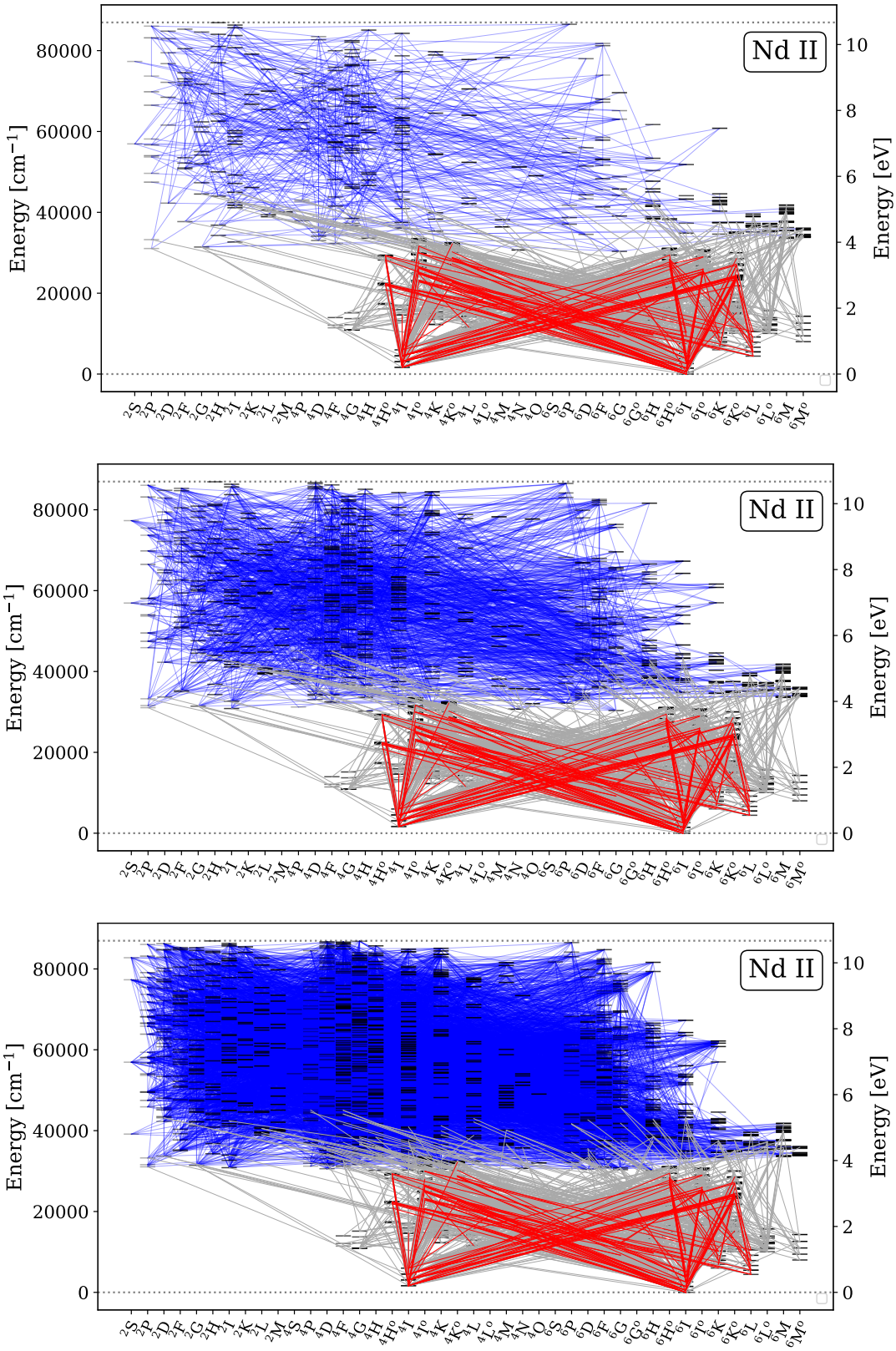

Figure 4. Grotrian diagrams of Nd II for three model atoms: atom A (top), atom B (middle), and atom C (bottom; see Section 2.4 for details on the atoms). Dotted lines indicate the ground state and ionization energy of Nd II. The 122 transitions of interest shown in Figure 1 are also highlighted here in red. Transitions are highlighted in blue if their lower energy level is theoretical.

as $T_{\rm eff}$ changes. As expected, we find relatively small $\Delta A_{\rm NLTE}$ values, increasing from roughly -0.1 to 0.1 dex as $T_{\rm eff}$ increases from 7500 K to 8000 K.

Additionally, we added hyperfine structure (HFS) and isotopic splitting data for six Nd II lines from I. U. Roederer et al. (2008) to our model atom to investigate the impacts of

Table 2
Mean Non-LTE Corrections for the Sun and HD 222925 Calculated from Model Atoms Supplemented with Theoretical Data

	$\Delta A_{\rm NLTE}$ (Sun)	$\Delta A_{\rm NLTE}$ (HD 222925)
Experimental Data Only	0.101 ± 0.017	0.168 ± 0.052
Atom A (+251 levels)	0.099 ± 0.017	0.165 ± 0.050
Atom B (+515 levels)	0.099 ± 0.017	0.165 ± 0.087
Atom C (+1055 levels)	0.098 ± 0.016	0.165 ± 0.088

HFS and isotopic splitting on NLTE abundance analysis, which have previously been assumed to be negligible (E. A. Den Hartog et al. 2003). Rederiving NLTE abundances for the Sun and HD 222925 with this model atom confirms this hypothesis; for both stars, the line-by-line Nd abundances changed by less than 0.005 dex, and so we proceed without further implementation of the HFS data and isotopic splitting.

3. Non-LTE Abundance Analysis

In this section, we discuss our NLTE analysis of Nd spectral lines in a small sample of stars, before proceeding with the computation of a larger grid of NLTE corrections. We begin by comparing synthetic spectra generated with our Nd model atom to observed stellar spectra, and then we present NLTE abundances of a small sample of stars to demonstrate the necessity of further analysis. From here, we provide details on the creation of a grid of model atmospheres for FGK stellar parameters, and the calculation of NLTE corrections at each point within this grid.

3.1. Non-LTE Synthetic Spectra

We generated synthetic spectra from our model atom using TS-NLTE in order to compare with existing observations of stars. We used the Python wrapper `TSFitPy` to run TS-NLTE in LTE and NLTE (J. M. Gerber et al. 2023; N. Storm & M. Bergemann 2023) with 1D MARCS model atmospheres. We implemented isotopic ratios of neutron-capture elements up to europium ($Z = 63$) from C. Sneden et al. (2008) in `TSFitPy`. Our atomic line lists for synthesizing and fitting the spectral regions around Nd II lines of interest come from Gaia ESO (U. Heiter et al. 2021).

For the solar synthetic spectra, we use $\xi_t = 0.85$ km s^{-1} and a macroturbulent velocity of 3 km s^{-1} (A. P. Doyle et al. 2014). For the synthetic spectra of HD 222925, we adopt $\xi_t = 2.2$ km s^{-1} from I. U. Roederer et al. (2018), and a macroturbulent velocity of 7 km s^{-1} (I. U. Roederer, private communication). Figure 5 shows the generated synthetic spectra plotted over selected Nd II lines observed in the Sun and HD 222925. Details on the spectrum and stellar parameters for HD 222925 can be found in I. U. Roederer et al. (2018), and the solar spectrum was taken in 2016 with the Potsdam Echelle Polarimetric and Spectroscopic Instrument (K. G. Strassmeier et al. 2018). In this figure, we show wavelength ranges around Nd II spectral lines for both the Sun and HD 222925. To ensure the best fit to the synthetic spectra, we renormalize the observed spectra within each range in blended regions. The synthetic spectrum shown in each plot uses NLTE modeling for Nd II with the respective abundances we derived using `MULTI2.3`, and shaded regions showing a typical abundance uncertainty of 0.2 dex. LTE is assumed for all other elements; the solar abundances are from M. Bergemann et al. (2021) and E. Magg et al. (2022), and the mean abundances for HD 222925 are adopted from I. U. Roederer et al. (2018). Some of these lines are blended, but a synthetic spectrum with no Nd (shown as a dashed line) is also included to demonstrate the contribution of Nd to each spectral feature. By visual inspection, it can be seen that the Nd II lines in our synthetic spectra agree fairly well with the observed spectrum. Thus, we are confident that our model atom is capable of reproducing synthetic spectra (using previously published stellar parameters) that agree with observational data, and so we proceed with more detailed NLTE analysis.

3.2. Application to Metal-poor Stars

After testing our NLTE model atom for the Sun and a metal-poor *r*-process-enhanced benchmark star (HD 222925), we proceed to use our model to derive NLTE abundances for a sample of metal-poor stars with previously measured Nd II LTE abundances from the literature. The list of stars chosen is given in Table 3 along with their stellar parameters from referenced literature sources. Uncertainties on stellar parameters are also taken from the papers in the table; if no uncertainty is provided in the paper, we instead adopt the typical value provided by the paper for each stellar parameter. LTE and NLTE Nd II abundances were derived for each star from the observed EWs collected from the literature as listed in Table 3. Most of these studies list a typical EW uncertainty on the order of ∼1 mÅ, but do not report a measurement uncertainty for every individual line. For the Sun and HD 222925, we performed robustness tests, increasing and decreasing each reported EW by a conservative uncertainty estimate of 10% to observe how the derived abundance changes. We find that this produces an abundance uncertainty of ∼0.05 dex. As this is lower than the typical stellar abundance uncertainties, we expect that other factors such as the choice of model and stellar parameters likely have a larger effect on the overall line-by-line uncertainty for our sample.

Abundances were derived using stellar parameters from the references listed in Table 3, and MARCS model atmospheres corresponding to the parameters of each star. For each star, we adopt typical uncertainties from the same paper as stellar parameters, if no uncertainties are reported. For stars with six or more measured EWs, we provide the standard deviation of the line-by-line abundances as the uncertainty on A(Nd); for stars with fewer than six measurements, we instead adopt a typical uncertainty of ±0.2 dex (for HD 122563, we adopt ±0.1 dex due to the higher signal-to-noise ratio of the observations). For most stars, EW measurements were available and used to derive line-by-line A(Nd) abundances using COGs as described in Section 2.3. However, whenever observed EWs were not available, we instead used the COG method to synthetically derive EWs at the corresponding LTE abundances, which were then used to derive NLTE abundances for these lines. We note that these values do not necessarily represent real EWs measured directly from spectra, which limits the accuracy of the corrections for these stars. The purpose of this method is to obtain preliminary $\Delta A_{\rm NLTE}$ values for a few stars of interest to better probe the necessity of further NLTE analysis. For all EWs used, the reduced EW (REW; $\log(EW/\lambda)$) falls on the roughly linear portion of the COG, which is most reliable for this method of analysis.

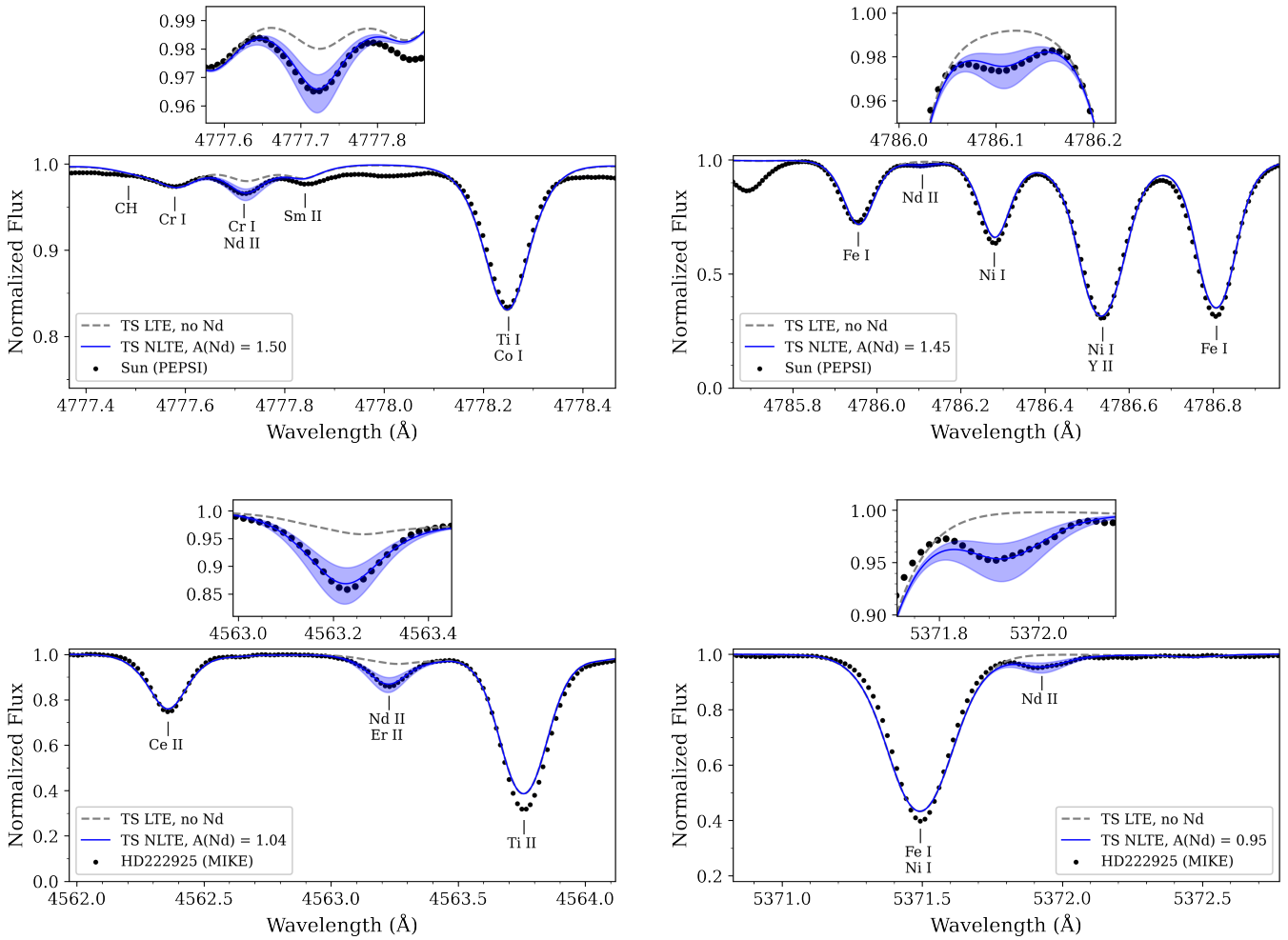

Figure 5. Observed and synthetic spectra for wavelength regions around two solar Nd II lines (top) and two Nd II lines in HD 222925 (bottom). For HD 222925, the abundances were obtained and synthetic spectra were generated using the stellar parameters listed in I. U. Roederer et al. (2018). Shaded regions indicate ±0.2 dex in the NLTE abundance. Prominent spectral lines and features are labeled. Small panels above each plot are zoomed in on the Nd II lines under consideration.

Table 3
Benchmark Stars for the Non-LTE Abundance Analysis of Nd II Lines

Star	N	$A(\mathrm{Nd})_{\mathrm{LTE}}$	$A(\mathrm{Nd})_{\mathrm{NLTE}}$	T_{eff} (K)	$\log g$	[Fe/H]	ξ_t (km s^{-1})	References
Sun	25	1.34 ± 0.05	1.44 ± 0.05	5777	4.44	0.00	0.85	(1)
HD 115444	34	−1.16 ± 0.08	−0.91 ± 0.07	4650 ± 150	1.50 ± 0.50	−2.99 ± 0.50	2.10 ± 0.30	(1, 2)[a]
BD+17°3248	55	−0.10 ± 0.07	0.11 ± 0.07	5200 ± 150	1.80 ± 0.30	−2.00 ± 0.20	1.90 ± 0.20	(1, 3)[a]
CS22892–052	35	−0.42 ± 0.06	−0.14 ± 0.08	4828 ± 150	1.35 ± 0.30	−3.08 ± 0.11	2.15 ± 0.30	(1, 4)[a]
HD 122563	1	−1.88 ± 0.10	−1.59 ± 0.10	4620 ± 92	1.21 ± 0.23	−2.76 ± 0.07	1.89 ± 0.08	(5, 6)[a]
CS30306–132	6	−0.36 ± 0.07	−0.18 ± 0.06	5100 ± 100	2.20 ± 0.30	−2.50 ± 0.20	1.90 ± 0.30	(5)
J0326+0202	1	−1.43 ± 0.20	−1.23 ± 0.20	5080 ± 100	2.03 ± 0.30	−3.11 ± 0.20	2.01 ± 0.30	(7)
J1108+2530	2	−0.93 ± 0.20	−0.79 ± 0.20	5003 ± 100	2.05 ± 0.30	−2.72 ± 0.20	1.08 ± 0.30	(7)
J1256+3440	2	−1.10 ± 0.20	−0.88 ± 0.20	5215 ± 100	1.74 ± 0.30	−2.76 ± 0.20	2.37 ± 0.30	(7)
HD 222925	98	0.72 ± 0.06	0.89 ± 0.06	5505 ± 80	2.39 ± 0.14	−1.55 ± 0.09	2.34 ± 0.09	(8)[b],[c]
HD 49368	3	2.20 ± 0.20	2.18 ± 0.20	3679 ± 70	0.35 ± 0.08	−0.19 ± 0.04	1.66 ± 0.25	(9)[c]
HD 35155	3	3.42 ± 0.20	3.17 ± 0.20	3656 ± 70	0.24 ± 0.08	−0.72 ± 0.04	1.66 ± 0.25	(9)[c]

Notes.
[a] EWs adopted from the first reference, stellar parameters adopted from the second reference.
[b] Parameters recalculated in NLTE using LOTUS (Y. Li & R. Ezzeddine 2023) to reduce trends in the line-by-line abundances.
[c] EW measurements derived from LTE abundances using a COG.
References. (1) E. A. Den Hartog et al. (2003), (2) J. Westin et al. (2000), (3) J. J. Cowan et al. (2002), (4) A. Frebel et al. (2013), (5) W. Aoki et al. (2005), (6) Y. Li & R. Ezzeddine (2023), (7) M. K. Mardini et al. (2019), (8) I. U. Roederer et al. (2018), and (9) S. Hasselquist et al. (2016).

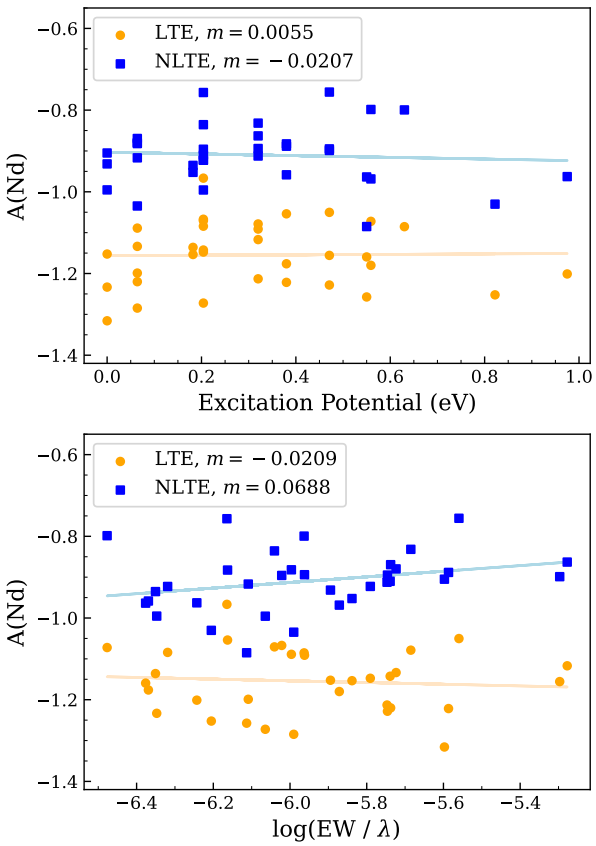

Figure 6. Line-by-line A(Nd) vs. EP (top) and REWs (bottom) for HD 115444, with lines of best fit for both LTE and NLTE (slopes given in the legend). The LTE abundance is $A(\mathrm{Nd})_{\mathrm{LTE}} = -1.155 \pm 0.079$, and the NLTE abundance is $A(\mathrm{Nd})_{\mathrm{NLTE}} = -0.910 \pm 0.073$.

Upon inspecting the line-by-line Nd II abundance trends as a function of excitation potential (EP) and line strengths ($\log(\mathrm{EW}/\lambda)$), we find that the best-fit line has a slope close to zero for most stars, for both LTE and NLTE, as demonstrated for HD 115444 in Figure 6. It is noteworthy to mention, however, that for HD 222925 a trend was observed with a slope of −0.079 obtained for the NLTE line-by-line Nd II abundances versus EP, and of 0.068 versus REW. To investigate whether these trends are arising due to the adopted stellar parameters, we recompute T_{eff}, $\log g$, [Fe/H], and ξ_t using the NLTE stellar parameter optimization tool `LOTUS` (Y. Li & R. Ezzeddine 2023), employing measured EWs for Fe I and Fe II lines from I. U. Roederer et al. (2018). The derived NLTE stellar parameters are $T_{\mathrm{eff}} = 5505$ K, $\log g = 2.39$, $[\mathrm{Fe/H}] = -1.55$, and $\xi_t = 2.34$ km s^{-1}, which compare relatively well to those derived by I. U. Roederer et al. (2018): $T_{\mathrm{eff}} = 5636$ K, $\log g = 2.54$, $[\mathrm{Fe/H}] = -1.50$, and $\xi_t = 2.20$ km s^{-1}. We then rederive the Nd II abundances using the new parameters, where we find that the overall NLTE abundance trend slopes decrease to −0.046 (for EP) and 0.025 (for line strengths). Notably, these slopes are larger than those obtained for the LTE line-by-line abundances using the I. U. Roederer et al. (2018) parameters, where slopes of 0.015 (versus EP) and 0.007 (versus REW) were computed.

It is possible that the slope trends in NLTE are due to 3D model atmospheric effects, which have been shown to introduce abundance trends as a function of EP for a number of elements studied in 3D NLTE, such as iron (A. M. Amarsi et al. 2022; Y. Li & R. Ezzeddine 2023) and magnesium (M. Bergemann et al. 2017). Low-EP lines are shown to be especially affected by ignoring 3D modeling effects. We are unable to diagnose these trends using a full 3D, NLTE analysis for Nd as it is beyond the scope of this current work and computationally expensive. Additionally, while some ⟨3D⟩ NLTE models are publicly available for a limited number of stellar parameters (J. M. Gerber et al. 2023), they are not available for stellar models of many giant stars with $T_{\mathrm{eff}} \geqslant 5000$ K (Z. Magic et al. 2013), and so ⟨3D⟩ NLTE analysis cannot be tested for HD 222925. We thus warrant that a future full 3D, NLTE analysis is needed to fully investigate these trends, and suggest the adoption of 1D, NLTE abundances instead of 1D, LTE for now as they are more physically motivated.

We compute ΔA_{NLTE} for each star in our sample as a function of stellar parameters to investigate the magnitude of NLTE effects, as shown in Figure 7. The S-type stars HD 35155 and HD 49368, with spectral lines measured in the H band from S. Hasselquist et al. (2016), have negative NLTE corrections, whereas the stars with spectral lines bluer than 5900 Å have positive NLTE corrections. Based on these measurements, ΔA_{NLTE} for optical lines appears to increase as [Fe/H], $\log g$, and T_{eff} decrease. The discrepancy in the ΔA_{NLTE} values and trends between different wavelength ranges is evidence that the NLTE correction for Nd varies significantly depending not only on stellar parameters, but also spectral line properties. We thus perform calculations for a larger range of stellar parameters and spectral lines to thoroughly investigate trends in ΔA_{NLTE} versus various stellar and line parameters.

3.3. Non-LTE Correction Grid

We selected a parameter space typical of FGK-type metal-poor stars in which to calculate ΔA_{NLTE} corrections for 122 Nd II lines that have previously been measured in these stars. Properties of these 122 transitions are given in Appendix Table A2. Our grid of stellar parameters covers the ranges $4000\ \mathrm{K} \leqslant T_{\mathrm{eff}} \leqslant 6500$ K (step size 250 K), $0.50 \leqslant \log g \leqslant 4.50$ (step size 0.2 dex), $-3.00 \leqslant [\mathrm{Fe/H}] \leqslant -1.00$ (step size 0.25 dex), and $1\ \mathrm{km\ s^{-1}} \leqslant \xi_t \leqslant 2\ \mathrm{km\ s^{-1}}$ (step size 1 km s^{-1}). Due to unreliable interpolation between atmospheric models, a small number of combinations of $\log g$ (below 1.00 dex) and T_{eff} (above 6000 K) were omitted from the grid, but we do not expect many stars of interest to fall within this region of parameter space.

For each of these sets of stellar parameters, a generalized COG (GCOG) was generated for each spectral line of interest using the method described in Section 2.3 with a higher-order polynomial to fit a larger number of Nd abundances. To avoid excessive computing time and convergence errors while still covering stars of interest for r-process research, we selected a set of A(Nd) values for each metallicity as shown in Figure 8. The general parameter space covered by the grid was chosen by referencing literature data from JINAbase (A. Abohalima & A. Frebel 2018).

In total, we ran `MULTI2.3` for 54,450 combinations of T_{eff}, $\log g$, [Fe/H], ξ_t, and A(Nd). For each of the sets of stellar parameters described above, we created GCOGs by fitting a degree-five polynomial to the `MULTI2.3` EW output for between 11 and 17 A(Nd) values (shown in Figure 8), in both NLTE and LTE for each spectral line. Interpolation with a lower-order polynomial over a smaller neighborhood of grid

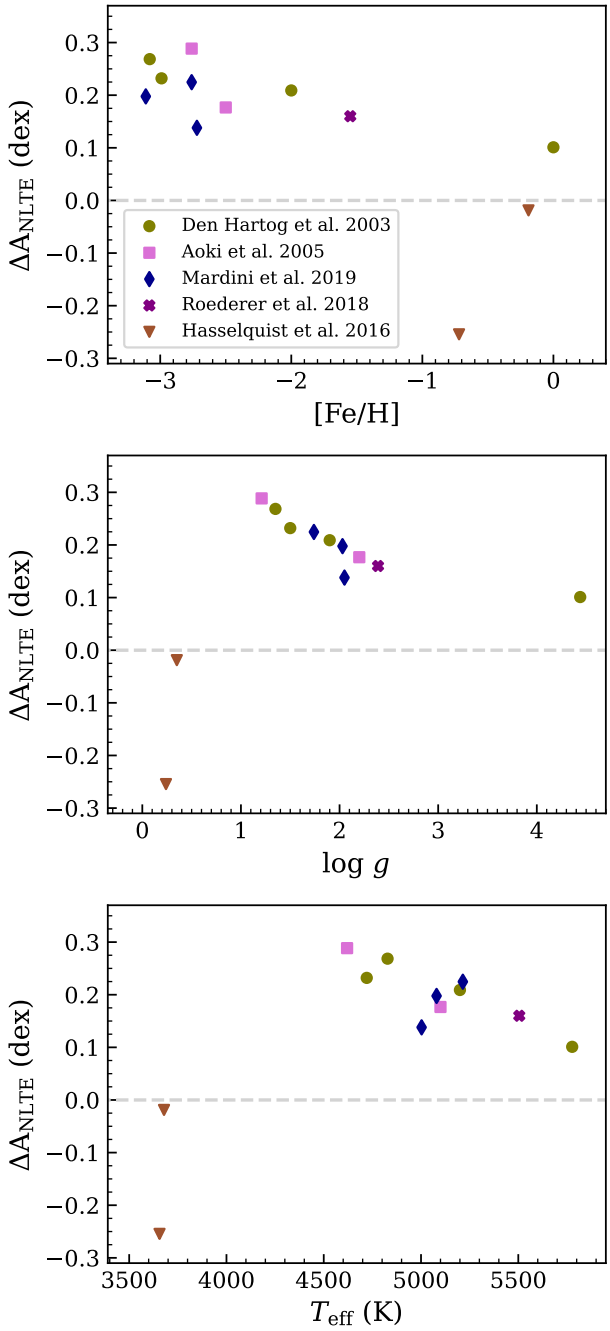

Figure 7. Plots of $\Delta A_{\rm NLTE}$ vs. [Fe/H] (top), $\log g$ (middle), and $T_{\rm eff}$ (bottom) for the stars in Table 3. Each point represents the mean $\Delta A_{\rm NLTE}$ value calculated using spectral line measurements from a single paper.

points would produce similar results, but as we demonstrate in the following section, our chosen method is sufficiently precise and accurate. We then determined $\Delta A_{\rm NLTE}$ from the abundance difference between the LTE and NLTE GCOGs at the LTE EW corresponding to each grid point. To create a useful grid, we compiled a list of all Nd II lines that had been measured at least once in our sample of stars (see Section 3.2), as well as five additional H-band lines from S. Hasselquist et al. (2016). This results in a 6D grid containing $\Delta A_{\rm NLTE}$ for each set of parameters $T_{\rm eff}$, $\log g$, [Fe/H], ξ_t, $A({\rm Nd})_{\rm LTE}$, and spectral line wavelength λ.

3.4. Testing Grid Interpolation Accuracy

Having generated a grid of evenly spaced $\Delta A_{\rm NLTE}$ values within a large parameter space, we aim to demonstrate that linear interpolation between precalculated grid points produces sufficiently accurate NLTE corrections for the 122 selected Nd II spectral lines at most stellar parameter combinations. We thus interpolate NLTE corrections for each spectral line for nine stars from Table 3, excluding the two S-type stars (HD 49368 and HD 35155) and the Sun, as their parameters fall significantly outside of the grid. While some stars fall slightly outside the grid with [Fe/H] $\geqslant -3.11$ or

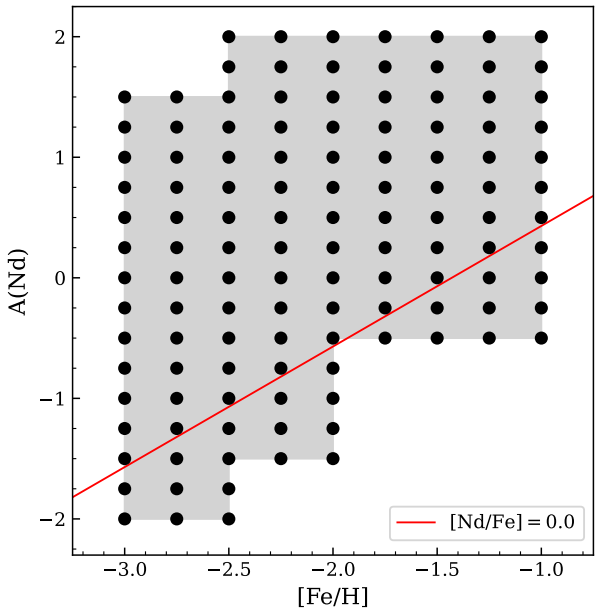

Figure 8. A grid displaying all values of $A(\mathrm{Nd})_{\mathrm{LTE}}$ chosen for each metallicity value in our parameter space ($-3.0 \leqslant [\mathrm{Fe/H}] \leqslant -1.0$). A line showing [Nd/Fe] = 0 is provided for reference.

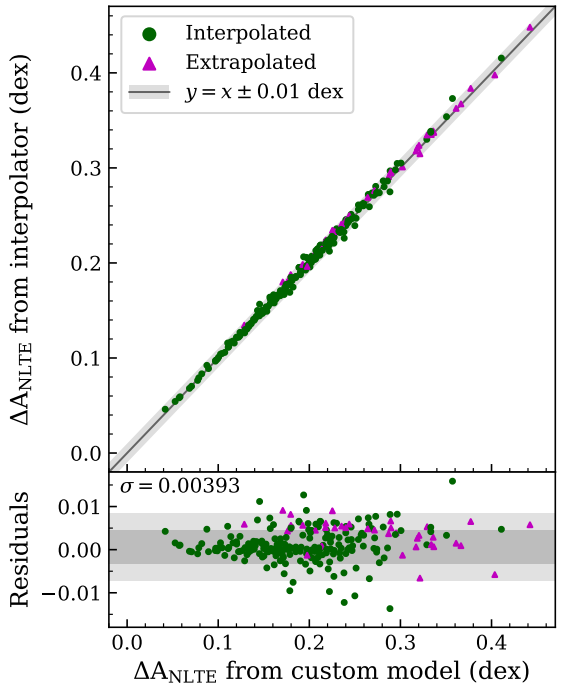

Figure 9. Comparison of ΔA_{NLTE} calculation methods for 248 measurements of optical Nd II lines in FGK stars. Interpolated points are shown as green circles, and extrapolated points are shown as purple triangles. A shaded region is included to highlight points that are within 0.01 dex of exact agreement. Residuals from the one-to-one line are shown ($\mu = 0.00140$, $\sigma = 0.00393$) with shaded regions indicating $\pm 1\sigma$ and $\pm 2\sigma$.

$\xi_t \leqslant 2.37$ km s^{-1}, their parameters are close enough to the grid range so we chose to extrapolate for their parameters. We then compare the interpolated NLTE corrections with the previously derived line-by-line NLTE corrections from Table 3. The comparisons are shown in Figure 9. The two methods produce nearly identical corrections for the spectral lines for all of the chosen stars, where the mean difference in ΔA_{NLTE} between the two methods is 0.001 dex, with a standard deviation of 0.004 dex. The largest difference is 0.016 dex, and 232 of the 238 interpolated values (97.5%) lie within 0.01 dex of the one-to-one line. This gives us confidence that linear interpolation within the parameter space of our grid will produce sufficiently accurate corrections for NLTE analysis of metal-poor stars.

4. Results and Discussion

In this section, we present an analysis of our results for the ΔA_{NLTE} calculations described in the sections above, focusing on NLTE corrections as a function of both stellar parameters and spectral line properties, as well as discussing implications for *r*-process-enhanced stars and comparison to results from the literature.

4.1. Variation of ΔA_{NLTE} with Stellar Parameters

With respect to the phase space of stellar parameters, the NLTE corrections for Nd II appear to be highly degenerate and interdependent. Figure 10 shows NLTE abundance corrections calculated from GCOGs for a sample of models from our grid. By fixing the stellar parameters to values corresponding to typical red giant ($\log g = 1.5$) and dwarf main-sequence ($\log g = 4.3$) stars, and plotting ΔA_{NLTE} versus $A(\mathrm{Nd})_{\mathrm{LTE}}$ and [Fe/H], respectively, for commonly measured optical and IR Nd II lines, we observe distinct trends for different types of stars and different lines. For optical lines in dwarf main-sequence stars, ΔA_{NLTE} is positive and relatively constant as $A(\mathrm{Nd})_{\mathrm{LTE}}$ and [Fe/H] vary (with typical values of $\Delta A_{\mathrm{NLTE}} = 0.1$), only decreasing slightly to $\Delta A_{\mathrm{NLTE}} \simeq 0.05$ for highly Nd-enhanced stars ($A(\mathrm{Nd})_{\mathrm{LTE}} \gtrsim 1.5$). NIR lines in the *H* band have a roughly constant negative correction of $\Delta A_{\mathrm{NLTE}} = -0.04$ dex, although we note that the NIR spectral lines for many main-sequence FGK parameters are far too weak to observe.

We find that for the model red giant star, ΔA_{NLTE} is typically larger than that for the model dwarf and depends on both $A(\mathrm{Nd})_{\mathrm{LTE}}$ and [Fe/H]. Stars with $A(\mathrm{Nd}) \lesssim 0$ have roughly constant NLTE corrections of 0.2 dex, while stars with $A(\mathrm{Nd}) \gtrsim 0$ display a sharp decrease in NLTE corrections for the optical lines toward $\Delta A_{\mathrm{NLTE}} = 0$, as $A(\mathrm{Nd})_{\mathrm{LTE}}$ increases. Corrections for the *H*-band lines, on the other hand, slightly increase from -0.07 to 0.00 dex as $A(\mathrm{Nd})_{\mathrm{LTE}}$ increases. For a fixed value of $A(\mathrm{Nd})_{\mathrm{LTE}} = -0.5$, we find that NLTE corrections decrease from 0.30 to 0.15 dex for the optical lines, and from -0.02 to -0.08 dex for the *H*-band lines, as [Fe/H] increases. The trends in ΔA_{NLTE}, particularly for giants, show a degeneracy with both metallicity and $A(\mathrm{Nd})$. As exemplified in the bottom panels of Figure 10 (particularly for optical lines in giants), for grid points where $\log(\mathrm{EW}/\lambda) \gtrsim -5.0$, there is a sharp change in the slope of ΔA_{NLTE} versus REW for each spectral line. Thus, the degeneracy is likely caused by saturation effects for Nd II lines with an REW above -5, as has been previously observed for other metals (K. Lind et al. 2011; H. Reggiani et al. 2019; A. M. Amarsi et al. 2022; C. Lagae et al. 2025). In this region of the parameter space, we expect the corrections to be less reliable due to differences in the COG slope and saturation point between NLTE and LTE models.

To further demonstrate trends within the NLTE correction grid, we compute ΔA_{NLTE} corrections for each line in our sample of 122 Nd II lines, as a function of T_{eff}, $\log g$, [Fe/H],

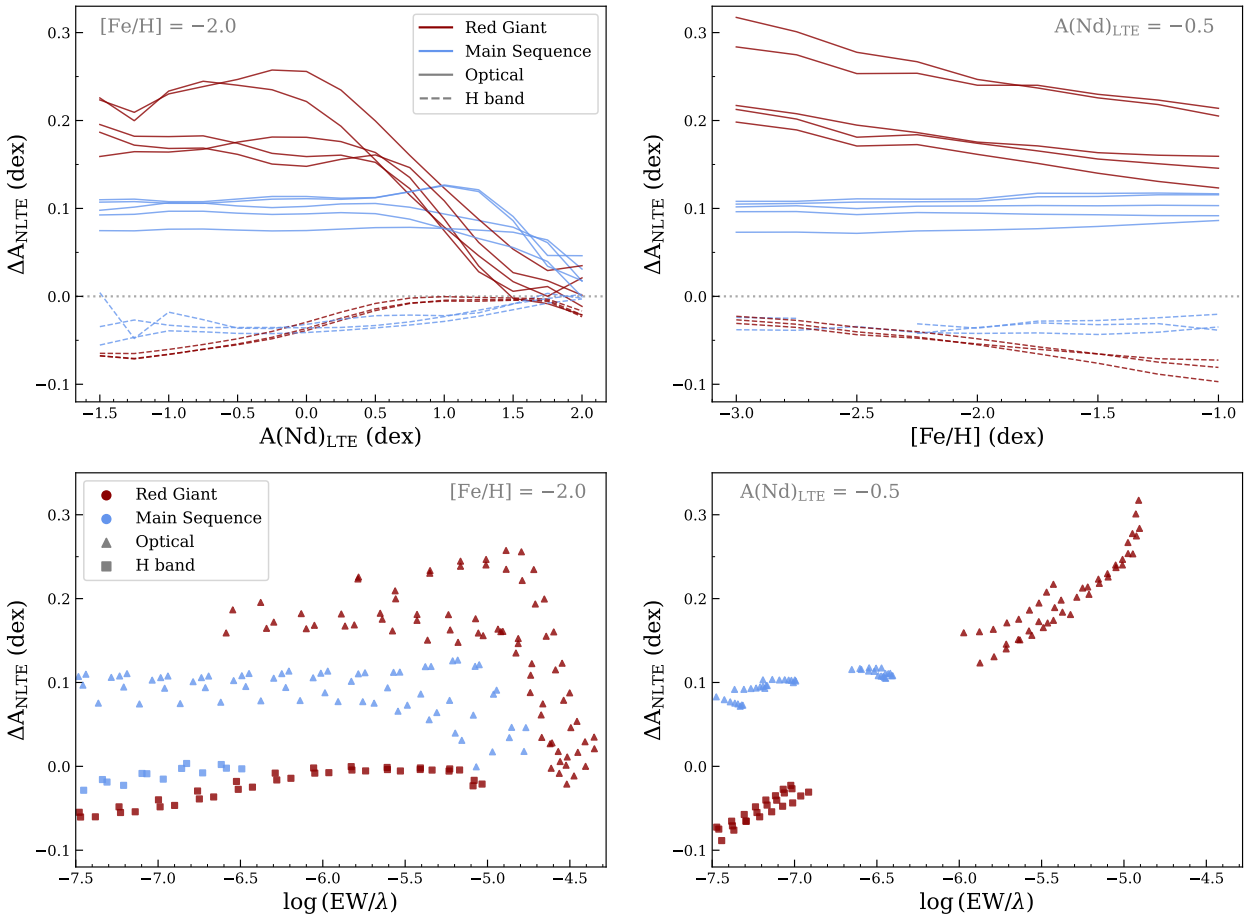

Figure 10. NLTE corrections as a function of $A(\mathrm{Nd})_{\mathrm{LTE}}$ (top left) and [Fe/H] (top right). Five commonly measured optical lines (4061.080, 4109.447, 4462.979, 5255.504, and 5319.813 Å) and three *H*-band lines (15368.118, 16053.616, and 16262.042 Å) are shown in each graph. With the exception of the parameter being varied, the dark red lines were calculated with typical red giant parameters ($T_{\mathrm{eff}} = 4250$ K, $\log g = 1.50$, [Fe/H] $= -2.0$, $\xi_t = 2.0$ km s^{-1}, and $A(\mathrm{Nd}) = -0.50$) and light blue lines were calculated with typical dwarf parameters ($T_{\mathrm{eff}} = 5750$ K, $\log g = 4.30$, [Fe/H] $= -2.0$, $\xi_t = 1.0$ km s^{-1}, and $A(\mathrm{Nd})_{\mathrm{LTE}} = -0.50$). The bottom panels show the same data points as the top panels, but with REW plotted on the horizontal axis. A lower limit of $\log(\mathrm{EW}/\lambda) = -7.5$ is chosen to make the effects of saturation above $\log(\mathrm{EW}/\lambda) \gtrsim -5.0$ more visible.

and A(Nd), as shown in the heat maps of Figure 11 for a number of lines across a range of wavelengths in the optical and NIR. The plots only display ΔA_{NLTE} in the regions of parameter space where the REW lies between -4.5 and -7, which is a typical range used for analysis with the COG method. As mentioned above, Nd II lines with an REW above -5 are not as reliable due to potential saturation issues. Our sample of observations from Section 3 does not appear to suffer from these issues, as Nd II lines are weak in most stars, and the small handful of strong lines observed in highly *r*-process-enhanced stars do not show unusual trends in ΔA_{NLTE}. However, we note this loose upper limit on line strength as a point of caution when performing NLTE abundance analysis of stars with high *r*-process enrichment.

We find that among blue lines ($\lambda < 4500$ Å), the NLTE corrections generally tend to be larger (up to $+0.5$ dex) for cooler giants with lower $\log g$ values and lower metallicities. Among those giants, the largest corrections are obtained for lower temperatures around 4000–4500 K. We also find that the corrections decrease as A(Nd) increases from -2 to $+2$, where they become close to zero for most parameters.

For optical lines with $4500 < \lambda < 6000$ Å, we find that for stars with $A(\mathrm{Nd})_{\mathrm{LTE}} < 1$, ΔA_{NLTE} increases up to 0.3 for warmer giant stars ($T_{\mathrm{eff}} > 5000$ K and $\log g < 2$), while remaining <0.1 for the rest of parameters. For $A(\mathrm{Nd}) = +2.0$, ΔA_{NLTE} can decrease down to -0.1. For NIR lines in the *H* band ($\lambda > 14000$ Å), we find that the corrections are negative, decreasing down to -0.3 for warmer ($T_{\mathrm{eff}} > 5000$ K) giants.

To investigate these large variations in NLTE effects for different stars, we present plots of departure coefficients $\beta_i = n_{i,\mathrm{NLTE}}/n_{i,\mathrm{LTE}}$ (the ratio of the population of an energy state i in NLTE versus LTE) as a function of optical depth. The top left, bottom left, top middle, and bottom middle panels of Figure 12 show β_i values in four model stars for three spectral lines: $\lambda = 3665$ Å (EP $= 0.205$ eV), $\lambda = 5319$ Å (EP $= 0.550$ eV), and $\lambda = 15368$ Å (EP $= 1.264$ eV). The four models represent a typical dwarf ($T_{\mathrm{eff}} = 5750$ K, $\log g = 4.3$, and $\xi_t = 1$ km s^{-1}) and red giant ($T_{\mathrm{eff}} = 4250$ K, $\log g = 1.5$, and $\xi_t = 2$ km s^{-1}) with [Fe/H] $= -3$ and -1.

As demonstrated in the top left and top middle panels of Figure 12, for a typical dwarf star, the upper levels of lower-EP optical and near-UV lines are overpopulated compared to LTE, and much more so than the lower levels. Thus, for the near-UV and optical lines, the source function is significantly larger than the Planck function ($J_\nu/B_\nu \simeq b_{\mathrm{upper}}/b_{\mathrm{lower}} > 1$), weakening the spectral line and explaining the slightly positive NLTE corrections, which compare well to studies of other dominant species (M. Bergemann & T. Nordlander 2014;

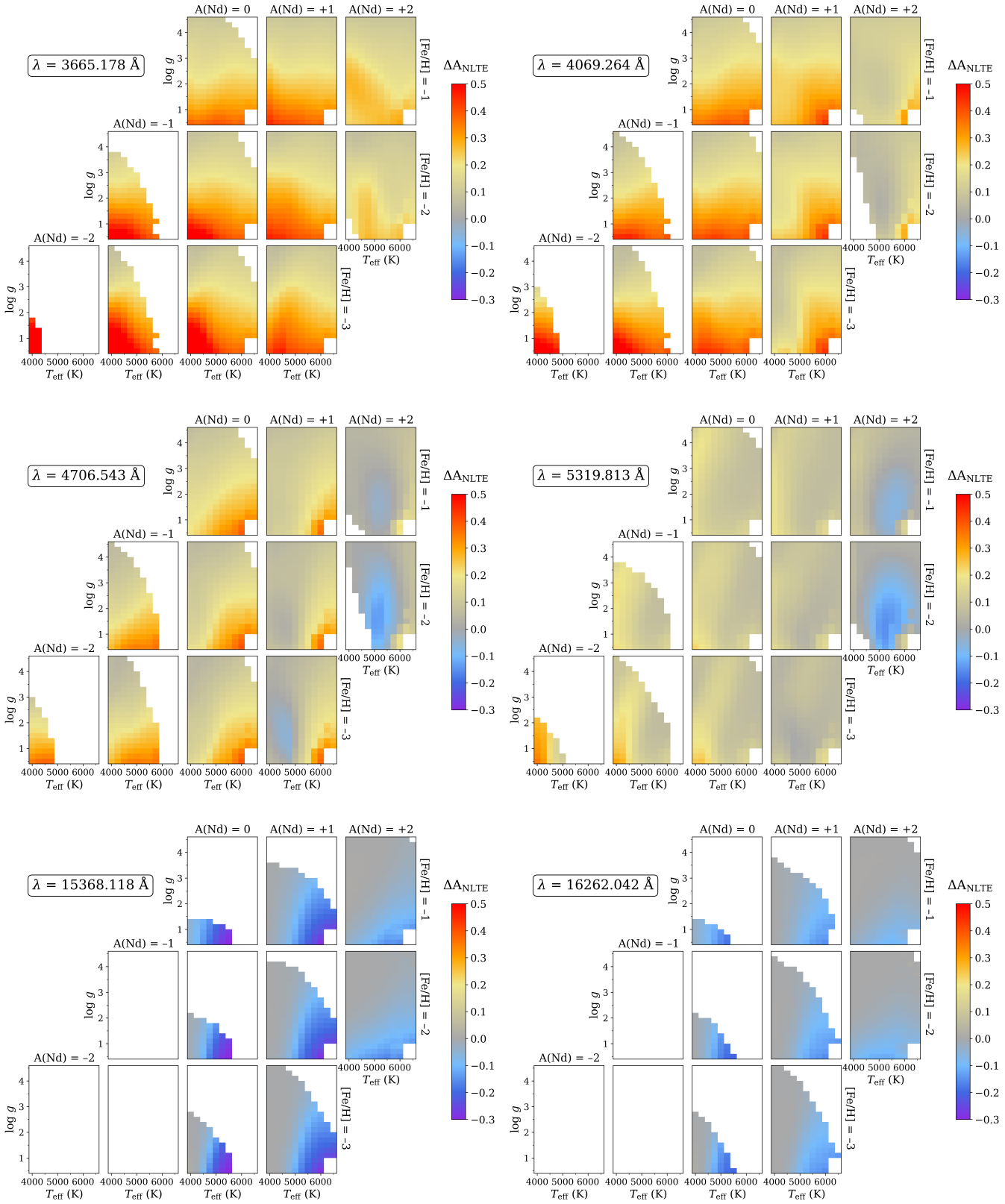

Figure 11. Heat maps of $\Delta A_{\rm NLTE}$ for six Nd II lines across the optical and NIR. Each individual panel in each heat map shows variations with $T_{\rm eff}$ and $\log g$ for a specific combination of [Fe/H] and $A({\rm Nd})_{\rm LTE}$ as indicated by the labels surrounding the panel. A value of $\xi_t = 1.5$ km s^{-1} is interpolated for all heat maps. Corrections are omitted if the interpolated model atmosphere was unreliable, or if the REW does not fall in the range $-7.0 \leqslant \log(W_\lambda/\lambda) \leqslant -4.5$.

N. Storm & M. Bergemann 2023). In the outer stellar atmosphere, the ratio $b_{\rm upper}/b_{\rm lower}$ is larger for the near-UV line than the optical, accounting for the slightly larger near-UV corrections in dwarf stars (as compared to redder optical lines) shown in Figure 11. Conversely for the NIR lines in dwarf stars, departure coefficients for the lower level slightly exceed

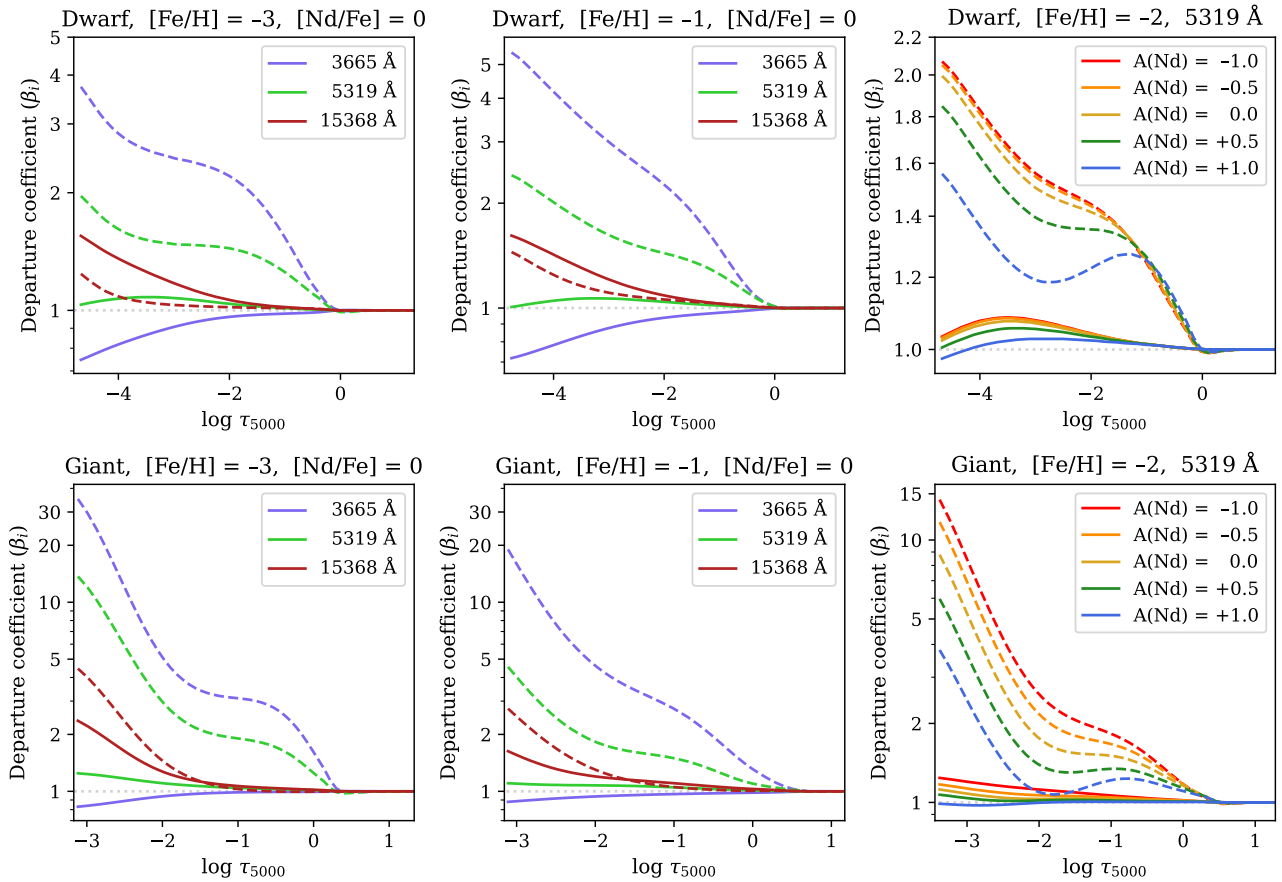

Figure 12. Departure coefficients as a function of optical depth at 5000 Å. The left and middle columns of panels show departure coefficients for the lower (solid) and upper (dashed) levels of a near-UV, optical, and NIR spectral line, for model atmospheres of a typical dwarf ($T_{\rm eff} = 5750$ K, $\log g = 4.3$, and $\xi_t = 1$ km s^{-1}) and giant ($T_{\rm eff} = 4250$ K, $\log g = 1.5$, and $\xi_t = 2$ km s^{-1}). The top right and bottom right panels show departure coefficients for a single optical line (5319 Å, EP = 0.55 eV) in both models at five different values of A(Nd).

those of the upper level, which is consistent with the negligible and slightly negative NIR corrections calculated for the dwarf star parameters in our grid.

The bottom left and bottom middle panels of Figure 12 explain the large NLTE corrections we see in near-UV and optical lines in giants as compared to those in the H band. Compared to dwarf stars, the departure coefficients for the lower levels of each line are similar, but the overpopulation in the upper levels is much more extreme. The ratio of $b_{\rm upper}/b_{\rm lower}$ is significantly higher than in the dwarf, and so the NLTE corrections will be positive and large. For the 3665 Å line at $\log \tau_{5000} = -3$, the departure coefficient is $\beta = 16$ for [Fe/H] $= -1$ and $\beta = 30$ for [Fe/H] $= -3$. This also shows that the departure from LTE in giants has a large dependence on metallicity, with more metal-poor giants having significantly stronger NLTE effects in the optical and near-UV. NLTE corrections are insignificant in the NIR for the stars chosen in Figure 12, but the effects of stellar parameters on $\Delta A_{\rm NLTE}$ in the H band can be seen more clearly in the bottom left and bottom right heat maps in Figure 11.

In the top right and bottom right panels of Figure 12, we show departure coefficients of the 5319 Å line at different A (Nd) values for both a typical dwarf and giant with [Fe/H] $= -2$. The difference in the departure coefficients between the upper and lower levels of the line explains why the calculated NLTE corrections are generally stronger for lower A (Nd) values regardless of the star type. This also appears to be true even for spectral lines with negative corrections; if departure coefficients for an energy level are less than one, the star with the highest A(Nd) abundance will generally have the largest departure coefficients (closest to unity).

4.2. Variation of ΔA_{NLTE} with Spectral Atomic Line Properties

As explained in the above sections, bluer near-UV Nd II lines tend to have overall more positive $\Delta A_{\rm NLTE}$ values, while redder Nd II lines (including H-band lines) have smaller and more negative corrections. To further investigate the dependence of the NLTE correction on spectral line properties, we plot $\Delta A_{\rm NLTE}$ versus both EP and wavelength for different sets of stellar parameters as shown in Figure 13. The plots show NLTE corrections for our sample of 122 Nd II lines, with different combinations of [Fe/H], $T_{\rm eff}$, $\log g$, and $A(\rm Nd)_{\rm LTE}$, for [Fe/H] $= -3$ and -1.5, $T_{\rm eff} = 4000$ K and 6000 K, $\log g = 1.5$ and 4.5, and $A(\rm Nd)_{\rm LTE} = -0.5$ and 1.5. Similarly as above, only lines corresponding to a REW between -7 and -4.5 are included. The plots clearly display the trends with wavelength discussed in Section 3 for metal-poor giants, where $\Delta A_{\rm NLTE}$ is highest for low-EP and bluer lines, and decreases or remains roughly constant as EP increases. For dwarf stars, regardless of the stellar parameters, $\Delta A_{\rm NLTE}$ remains a constant $\sim$0.1 dex as EP changes. The scatter in $\Delta A_{\rm NLTE}$ as a function of EP is also much smaller for dwarfs than giants. In giant stars, the corrections span a much wider

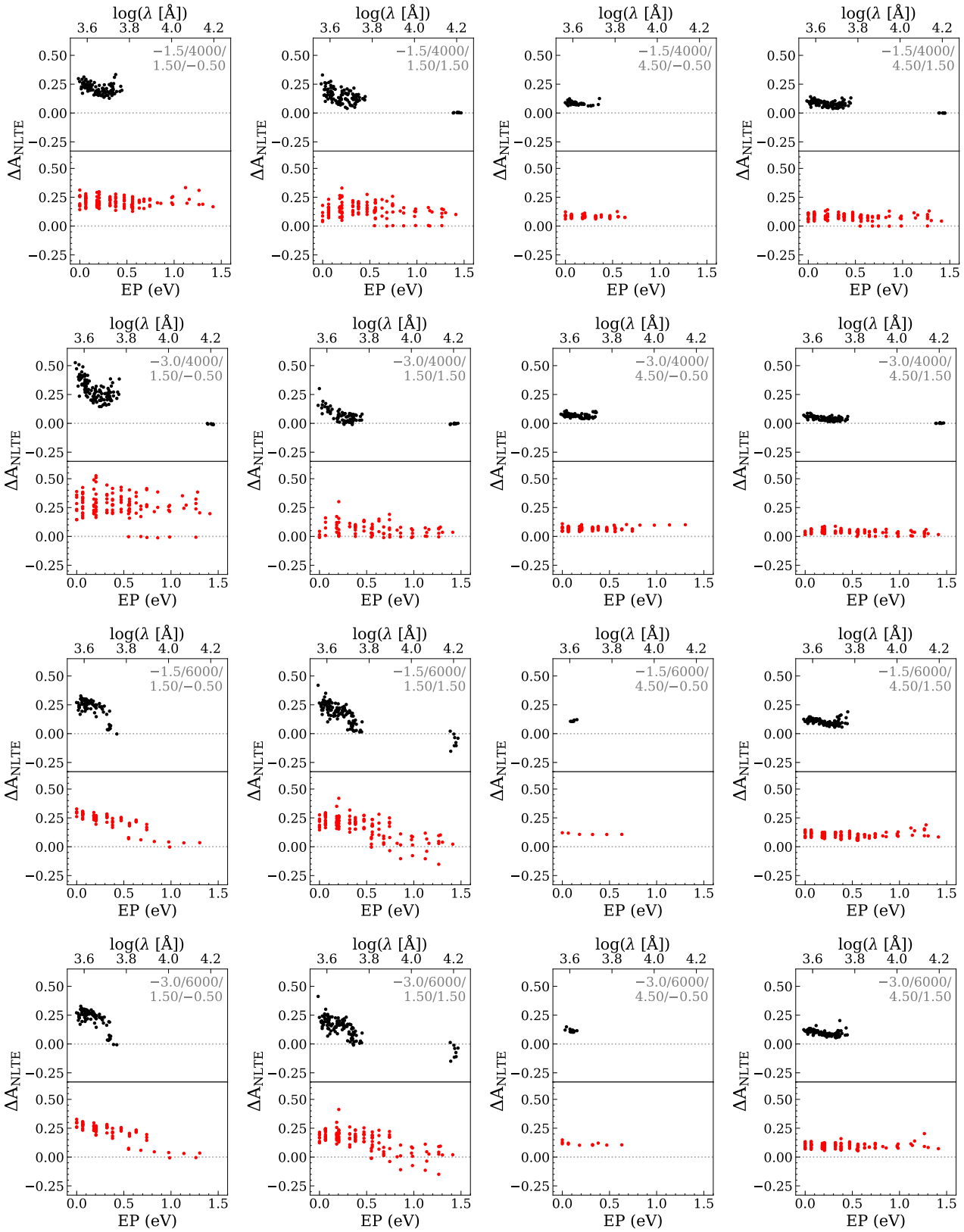

Figure 13. Plots of $\Delta A_{\rm NLTE}$ as a function of both wavelength (top) and EP (bottom) for 16 different combinations of stellar parameters [Fe/H], $T_{\rm eff}$ (K), $\log g$, and $A({\rm Nd})_{\rm LTE}$ near different extremes of the grid (indicated within each plot). We adopt $\xi_t = 2$ km s^{-1} for giant stars ($\log g = 1.5$) and $\xi_t = 1$ km s^{-1} for dwarf stars ($\log g = 4.5$). Hotter giant stars with the clearest negative trends are in the lower left quadrant. As with Figure 11, corrections are omitted if $\log(W_\lambda/\lambda) < -7$ or $\log(W_\lambda/\lambda) > -4.5$.

range, from −0.3 to 0.5 dex. Cooler giants have less of a downward trend with EP, and aside from the NIR lines, which have $\Delta A_{\rm NLTE} \simeq 0$ dex, $\Delta A_{\rm NLTE}$ values remain a constant 0.2 or 0.3 dex (depending on the star's metallicity and Nd abundance), with a large scatter. Hotter giant stars have the clearest downward trend, with low-EP lines having corrections

up to 0.3 dex and high EP lines having corrections as low as −0.3 dex

We also observe that NLTE effects are generally weaker for higher Nd abundances, independent of changes in stellar parameters, as shown in the top right and bottom right panels of Figure 12. Regardless if the NLTE corrections for a given star are positive or negative, they typically trend toward zero with increasing A(Nd).

These NLTE effects are likely caused by a complex combination of physical processes. When $J_\nu > B_\nu$ in the UV, overionization occurs, which primarily causes the populations of lower levels to decrease, especially in stars with low [Fe/H] and $\log g$ values. The analogous effect for bound–bound transitions is photon pumping, which can cause excess electrons from the lower level of a transition to populate the higher level if $J_\nu > B_\nu$ at the wavelength of the transition. Additionally, if $J_\nu < B_\nu$ in the infrared, a lack of ionization of higher-EP transitions will cause over-recombination of the upper energy levels (M. Bergemann & T. Nordlander 2014). The known effects of these processes on stellar abundance analysis generally align with the trends in $\Delta A_{\rm NLTE}$ that we observe with respect to EP, particularly for metal-poor giants. However, it is difficult to fully predict how various physical processes interact within a stellar atmosphere, and a complete diagnostic analysis of the physical causes of these NLTE effects is outside the scope of this work.

As mentioned in Section 3.2, a 3D, NLTE analysis may further help reduce the line-by-line trends seen as a function of EP and wavelength for many stars. In summary, we thus recommend the adoption of the 1D, NLTE abundance corrections to the commonly derived 1D, LTE abundances for r-process abundance analyses, particularly for metal-poor giants. We also recommend using moderate and high EP lines for abundance analysis of Nd whenever possible, as they will have smaller and more reliable NLTE corrections.

4.3. Implications for r-process Stars

Our NLTE corrections are comparable to previously computed NLTE corrections for dominant species of other neutron-capture elements. For example, a recent study by N. Storm & M. Bergemann (2023) found that NLTE corrections for Y II are as high as 0.4 dex for low-EP lines at parameters of [Fe/H] $\simeq -3$ and $\log g \simeq 1$. The corrections for Y II follow the same general trends we obtained for Nd II, increasing for lower EPs, lower $\log g$ values, and lower [Fe/H] values. We note that while the NLTE corrections can be larger than the typical systematic uncertainties, they are <0.2 dex for most parts of the parameter space for both Y II and Nd II.

Other recent papers find similar results for dominant species of common neutron-capture tracers. L. Mashonkina et al. (2023) compute a grid of corrections for one Sr II and Ba II spectral line, finding that NLTE corrections range from −0.2 to 0.4 dex, with large corrections derived for cool, metal-poor giant stars. For both of these lines, the NLTE corrections are also larger for lower abundances, matching our results for Nd II. Y. Guo et al. (2025) studied NLTE effects for two Eu II lines at 4129 Å and 6645 Å, computing positive corrections as high as 0.2 dex for the former and negative corrections as low as −0.1 dex for the latter. For both lines, the deviation from LTE is stronger at lower metallicities, and giants show the most significant corrections. This study also applies these corrections to derived LTE abundances of both lines for a sample of metal-poor stars, finding that the two NLTE abundance values are in much closer agreement than the previous LTE values.

Based on all of these recent findings, it is possible that previously reported LTE abundances from optical lines of Nd (and possibly other neutron-capture elements) have underestimated the abundances of r-process elements, particularly in giant metal-poor stars. While NLTE has been ignored for most previous studies, it is clear that NLTE calculations for each element must be performed for a wide range of parameters in order to assess the magnitudes of NLTE effects, even for dominant species like Nd II.

5. Conclusions

We present an NLTE abundance analysis of Nd II using a grid of 1D, NLTE corrections derived with the NLTE radiative transfer code `MULTI2.3`. We built an Nd model atom from up-to-date experimental Nd I and Nd II data and then calibrated the impact of hydrogen collisions using solar photospheric and meteoretic Nd abundances, determining $S_{\rm H} = 0.1$. We incorporated theoretically computed Nd II transitions into our atom to assess the impact of atom completeness on our NLTE abundances, finding that the lack of experimental levels above 46,000 cm^{-1} has a negligible impact on the calculated NLTE corrections.

With this model atom, we generated synthetic spectra that successfully reproduced observations of Nd II spectral features for the Sun and the well-studied r-II star HD 222925 (I. U. Roederer et al. 2018), as well as a sample of Nd-enhanced stars, for which we derived NLTE effects as large as ±0.3 dex for multiple spectral lines in both the optical and H band. Most abundances in our sample were calculated from lines bluer than 5900 Å, and these abundances showed clear trends of $\Delta A_{\rm NLTE}$ increasing as $T_{\rm eff}$, $\log g$, and [Fe/H] decrease. However, we find opposite effects for abundances calculated from H-band lines, yielding negative NLTE corrections. To address the dependence of NLTE effects on changes in stellar atmospheric parameters, we generated a large grid of $\Delta A_{\rm NLTE}$ corrections, covering parameters typical of FGK main-sequence and giant stars.

We find significant trends in $\Delta A_{\rm NLTE}$ within our grid, where corrections range from −0.3 to +0.5 dex depending on the stellar parameters and spectral lines, which demonstrate the necessity of NLTE modeling for abundance analysis of Nd II. For a typical red giant, the optical corrections are roughly ∼0.2 dex for stars with lower Nd abundances but sharply decrease as the abundance rises above A(Nd) $\simeq 0.5$. For a typical G-type main-sequence star, the optical NLTE corrections are typically ∼0.1 dex, as evidenced by the abundance analysis of the Sun shown in Section 2. The largest positive corrections (+0.5 dex) are for blue spectral lines ($\lambda < 4000$ Å) for the lowest values of $T_{\rm eff}$, $\log g$, and [Fe/H] in the grid. Negative corrections, as low as −0.3 dex, are seen in NIR H-band lines for combinations of low $\log g$ and high $T_{\rm eff}$. Corrections generally tend to decrease as spectral line wavelength increases, and the trends in $\Delta A_{\rm NLTE}$ across spectral lines show that lower-EP lines tend to have larger corrections than higher-EP lines, particularly in hotter giant stars. We anticipate the possibility that ignoring 3D effects could be contributing to the larger corrections for low-EP lines, and thus recommend adopting optical and NIR Nd lines with higher EPs for future r-process abundance analysis when possible.

The nonnegligible $\Delta A_{\rm NLTE}$ values determined for Nd II and other neutron-capture species like Y II (N. Storm & M. Bergemann 2023), Eu II (Y. Guo et al. 2025), Sr II, and Ba II (L. Mashonkina et al. 2023) at different stellar parameters are of high interest for *r*-process research. These findings may have important implications for Galactic archaeology, as LTE analysis of blue lines in cool giants may significantly underestimate neutron-capture enhancement. Further investigations of NLTE effects for more neutron-capture species in *r*-process-enhanced stars, particularly lanthanides and elements around the second *r*-process peak, are needed to assess the robustness of the corrections to the solar *r*-process pattern. This would allow more precise insights into the astrophysical conditions of the creation of these elements via the *r*-process.

Future efforts to expand this research will include continuing to improve the model atom as more experimental atomic data become available, as well as broadening the parameter range of our $\Delta A_{\rm NLTE}$ grid to include spectral types like M and S. The current bounds of our grid were chosen to provide the most utility for *r*-process research in the optical range, but it is clear from our results that NIR spectral lines in stars with $T_{\rm eff} < 4000$ K require detailed NLTE calculations as well, especially as more IR spectra are released by the Fifth-generation Sloan Digital Sky Survey, JWST, and other IR telescopes in the following years. We will also apply our NLTE corrections to a large sample of MW metal-poor stars to revisit the [Nd/Fe] trends compared to chemical evolution models, as well as investigate more NLTE corrections for other lanthanide *r*-process elements (R. Shi et al. 2025, in preparation).

Acknowledgments

We are grateful to the anonymous referee for their valuable feedback and suggestions that have helped to improve this paper. The authors acknowledge UFIT Research Computing for providing computational resources and support that have contributed to the research results reported in this publication. URL: UFRC.[14]

The authors would like to sincerely thank Dr. Ian Roederer and Dr. Jennifer Marshall for their valuable feedback and support during the research process. This research was completed with financial support provided by the Dr. Dionel Avilés '53 and Dr. James Johnson '67 Graduate Fellowship Program at Texas A&M University. R.E. acknowledges support from JINA-CEE (Joint Institute for Nuclear Astrophysics Center for the Evolution of the Elements), funded by the NSF under grant No. PHY-1430152, and support from NSF grant AST-2206263 and NASA Astrophysics Theory Program grant 80NSSC24K0899. This work also benefited from discussions at the 2024 Frontiers in Nuclear Astrophysics meeting at the University of Notre Dame and the Third Frontiers in Nuclear Astrophysics Summer School at Ohio University, supported by IReNA under NSF Grant OISE-1927130. This publication was supported by the George P. and Cynthia Woods Mitchell Institute for Fundamental Physics and Astronomy at Texas A&M University.

This work has made use of NASA's Astrophysics Data System Bibliographic Services; the arXiv.org[15] preprint server operated by Cornell University; the SIMBAD and VizieR databases hosted by the Strasbourg Astronomical Data Center (M. Wenger et al. 2000); the Atomic Spectra Database hosted by NIST; and the VALD database operated at Uppsala University, the Institute of Astronomy RAS in Moscow, and the University of Vienna. Atomic data compiled in the DREAM database (E. Biémont et al. 1999) were extracted via VALD (F. Kupka et al. 1999, and references therein).

Software: `matplotlib` (J. D. Hunter 2007), `MULTI2.3` (M. Carlsson 1986, 1992), `FORMATO3` (T. Merle et al. 2011), `Turbospectrum` (R. Alvarez & B. Plez 1998; B. Plez 2012), TS-NLTE + `TSFitPy` (J. M. Gerber et al. 2023; N. Storm & M. Bergemann 2023), `LOTUS` (Y. Li & R. Ezzeddine 2023), `wrapper_multi` (https://github.com/stormnick/wrapper_multi).

[14] https://www.rc.ufl.edu/
[15] https://arxiv.org/

Appendix
Additional Tables

We present additional data mentioned in the text above. Table A1 displays the 25 solar lines used to calibrate the S_H factor, along with the EW of each line and the abundance derived with the MARCS model atmosphere using LTE and four different non-LTE model atoms with different values of S_H. Table A2 displays properties of the 122 spectral lines of interest that are included in our non-LTE correction grid.

Table A1
Line-by-line Nd Abundance Values Interpolated from Derived Curves of Growth for Each Line, Using the Solar MARCS Model Atmosphere in Both LTE and Four Different Non-LTE Models with Different S_H Values

λ (Å)	W_λ (mÅ)	$A(\mathrm{Nd})_{\mathrm{LTE}}$	$A(\mathrm{Nd})_{\mathrm{NLTE}}$ $S_H = 1.0$	$A(\mathrm{Nd})_{\mathrm{NLTE}}$ $S_H = 0.1$	$A(\mathrm{Nd})_{\mathrm{NLTE}}$ $S_H = 0.01$	$A(\mathrm{Nd})_{\mathrm{NLTE}}$ $S_H = 0.001$
4007.429	4.5	1.2898	1.3446	1.3798	1.3900	1.3913
4021.326	11.4	1.2986	1.3751	1.4162	1.4282	1.4297
4059.950	5.9	1.2734	1.3587	1.3926	1.4007	1.4017
4136.745	1.3	1.2568	1.3495	1.3704	1.3742	1.3746
4156.077	22.5	1.2867	1.3769	1.4227	1.4374	1.4394
4284.509	5.5	1.2830	1.3491	1.3763	1.3823	1.3831
4446.382	9.5	1.3002	1.3810	1.4169	1.4263	1.4274
4465.592	2.1	1.3186	1.3803	1.4194	1.4326	1.4344
4497.257	0.7	1.3916	1.4381	1.4729	1.4838	1.4849
4567.604	1.3	1.3284	1.3985	1.4316	1.4408	1.4421
4645.761	1.9	1.2886	1.3355	1.3619	1.3676	1.3682
4715.585	4.0	1.4131	1.4803	1.5139	1.5240	1.5252
4763.615	0.9	1.2836	1.3528	1.3788	1.3854	1.3863
4777.716	1.4	1.4281	1.4704	1.5004	1.5086	1.5097
4786.108	1.2	1.3546	1.4031	1.4451	1.4605	1.4626
4797.153	2.6	1.3486	1.4278	1.4516	1.4547	1.4549
4914.378	3.2	1.2689	1.3384	1.3644	1.3710	1.3717
5063.722	1.3	1.3572	1.4528	1.4671	1.4605	1.4592
5234.193	4.5	1.3823	1.4586	1.4665	1.4645	1.4642
5255.504	5.9	1.3275	1.3913	1.4271	1.4377	1.4390
5293.162	8.9	1.3641	1.4594	1.4683	1.4618	1.4607
5306.457	0.9	1.4185	1.5363	1.5365	1.5284	1.5273
5311.453	2.0	1.3464	1.4726	1.4784	1.4695	1.4681
5319.813	8.7	1.3238	1.3982	1.4053	1.4027	1.4024
5371.925	2.5	1.4377	1.5124	1.5241	1.5184	1.5174
Mean abundance	⋯	1.335 ± 0.053	1.410 ± 0.056	1.436 ± 0.050	1.440 ± 0.048	1.441 ± 0.048

Note. Wavelengths and EWs are from VALD and E. A. Den Hartog et al. (2003), respectively. Mean A(Nd) abundances with uncertainties are given at the bottom of the table. More details on the source of information for each line are given in Table A2.
References. VALD, NIST, and E. A. Den Hartog et al. (2003).

Table A2
Wavelengths, Excitation Potentials, and log(*gf*) Values for the 122 Nd II Lines in the Non-LTE Correction Grid

λ (Å)	EP (eV)	log(*gf*)	λ (Å)	EP (eV)	log(*gf*)	λ (Å)	EP (eV)	log(*gf*)
3615.811	0.2046	−0.760	4135.321	0.6305	−0.070	4959.120	0.0636	−0.800
3665.178	0.2046	−0.660	4136.745	0.3802	−1.030	4987.161	0.7421	−0.790
3728.125[a]	0.1823	−0.500	4156.077[a]	0.1823	0.160	4989.419[a]	0.6804	−1.190
3738.056	0.5595	−0.040	4177.319[a]	0.0636	−0.100	5063.722	0.9756	−0.620
3759.794[a]	0.6305	−0.450	4211.289	0.2046	−0.860	5066.828	0.5595	−1.430
3763.471[a]	0.2046	−0.430	4232.374	0.0636	−0.470	5092.792	0.3802	−0.610
3780.382[a]	0.4714	−0.350	4284.509[a]	0.6305	−0.170	5130.585[a]	1.3039	0.450
3784.243[a]	0.3802	0.150	4303.571[a]	0.0000	0.080	5132.329	0.5595	−0.710
3784.845	0.0636	−1.040	4351.281[a]	0.1823	−0.610	5165.125	0.6804	−0.740
3810.477	0.7421	−0.140	4358.161[a]	0.3206	−0.160	5167.918	0.5595	−1.180
3826.409[a]	0.0636	−0.410	4368.630	0.0636	−0.810	5192.613[a]	1.1365	0.270
3838.980	0.0000	−0.240	4385.660[a]	0.2046	−0.300	5212.358	0.2046	−0.960
3879.541	0.3206	−0.210	4400.821[a]	0.0636	−0.600	5215.651	1.2640	−0.740
3887.867	0.0636	−0.780	4446.382	0.2046	−0.350	5234.193	0.5502	−0.510
3890.937	0.0636	−0.220	4451.978	0.0000	−1.100	5249.574[a]	0.9756	0.200
3891.507[a]	0.7421	−0.140	4462.979[a]	0.5595	0.040	5250.812[a]	0.7446	−0.720
3900.218[a]	0.4714	0.100	4465.058	0.0000	−1.360	5255.504	0.2046	−0.670
3927.098	0.1823	−0.590	4465.592	0.1823	−1.100	5273.424[a]	0.6804	−0.180
3990.097[a]	0.4714	0.130	4497.257	0.4714	−1.380	5293.162[a]	0.8229	0.100
3991.741[a]	0.0000	−0.260	4497.914	0.5595	−1.020	5303.197	0.3802	−1.430
3994.673	0.3206	0.040	4501.809	0.2046	−0.690	5306.457	0.8594	−0.970
4004.004	0.0636	−0.570	4506.582	0.0636	−1.040	5311.453[a]	0.9857	−0.420
4007.429	0.4714	−0.400	4541.267	0.3802	−0.740	5319.813[a]	0.5502	−0.140
4011.063	0.4714	−0.760	4542.600	0.7421	−0.280	5356.965[a]	1.2640	−0.280
4012.243[a]	0.6305	0.810	4563.219	0.1823	−0.880	5371.925[a]	1.4124	0.000
4012.697	0.0000	−0.600	4567.604	0.2046	−1.310	5431.514	1.1212	−0.470
4013.216	0.1823	−1.100	4645.761	0.5595	−0.760	5485.097	0.5502	−1.640
4018.822	0.0636	−0.850	4703.571	0.3802	−1.000	5485.693[a]	1.2640	−0.120
4021.326	0.3206	−0.100	4706.543	0.0000	−0.710	5688.518[a]	0.9857	−0.310
4023.005	0.5595	0.040	4709.714	0.1823	−0.970	5740.856[a]	1.1602	−0.530
4041.056	0.4714	−0.530	4715.585	0.2046	−0.900	5811.570	0.8594	−0.860
4043.594	0.3206	−0.710	4763.615	0.3802	−1.270	5842.364[a]	1.2816	−0.600
4051.140	0.3802	−0.300	4777.716	0.3802	−1.220	15284.438[b]	0.6804	−2.130
4059.950	0.2046	−0.520	4786.108	0.1823	−1.410	15368.118[b]	1.2640	−1.550
4061.080[a]	0.4714	0.550	4797.153	0.5595	−0.690	15912.275[b]	0.5502	−2.390
4069.264	0.0636	−0.570	4799.419	0.0000	−1.450	15977.939[b]	1.1212	−2.470
4075.111	0.2046	−0.480	4820.337	0.2046	−0.920	16053.616[b]	0.7446	−2.200
4075.272[a]	0.0636	−0.760	4825.476	0.1823	−0.420	16262.042[b]	0.9857	−1.990
4109.070	0.0636	−0.160	4859.025	0.3206	−0.440	16303.772[b]	0.8594	−2.110
4109.447[a]	0.3206	0.350	4902.036	0.0636	−1.340	16634.655[b]	1.1365	−2.370
4133.351[a]	0.3206	−0.490	4914.378	0.3802	−0.700	…	…	…

Notes. If no footnote is present next to a wavelength, the wavelength and log(*gf*) value for that transition were acquired from VALD, but information on the upper and/or lower levels was missing and filled in by cross referencing with the NIST Atomic Spectra Database (ASD).
[a] All spectral line information for the transition was acquired from VALD.
[b] Wavelengths, EPs, upper and lower energy levels, and log(*gf*) values acquired from S. Hasselquist et al. (2016).
References. VALD, NIST ASD, and S. Hasselquist et al. (2016).

ORCID iDs

John D. Dixon https://orcid.org/0000-0001-6168-3130
Rana Ezzeddine https://orcid.org/0000-0002-8504-8470
Yangyang Li https://orcid.org/0000-0002-9953-7929
Thibault Merle https://orcid.org/0000-0001-8253-1603
Manuel Bautista https://orcid.org/0000-0001-6837-3055
Yanjun Guo https://orcid.org/0000-0001-9989-9834

References

Abdelkawy, A. G. A., Shaltout, A. M. K., Beheary, M. M., & Bakry, A. 2017, MNRAS, 470, 4007
Abohalima, A., & Frebel, A. 2018, ApJS, 238, 36
Afşar, M., Sneden, C., & Wood, M. P. 2018, ApJ, 865, 44
Alvarez, R., & Plez, B. 1998, A&A, 330, 1109
Amarsi, A. M., Liljegren, S., & Nissen, P. E. 2022, A&A, 668, A68
Aoki, W., Honda, S., Beers, T. C., et al. 2005, ApJ, 632, 611
Arlandini, C., Käppeler, F., Wisshak, K., et al. 1999, ApJ, 525, 886
Bandyopadhyay, A., Ezzeddine, R., Allende Prieto, C., et al. 2024, ApJS, 274, 39
Bergemann, M. 2014, in Determination of Atmospheric Parameters of B-, A-, F- and G-Type Stars. Series: GeoPlanet: Earth and Planetary Sciences, ed. E. Niemczura, B. Smalley, & W. Pych (Cham: Springer), 187
Bergemann, M., Lind, K., Collet, R., Magic, Z., & Asplund, M. 2012, MNRAS, 427, 27
Bergemann, M., & Nordlander, T. 2014, in Determination of Atmospheric Parameters of B-, A-, F- and G-Type Stars. Series: GeoPlanet: Earth and Planetary Sciences, ed. E. Niemczura, B. Smalley, & W. Pych (Cham: Springer), 169
Bergemann, M., Collet, R., Amarsi, A. M., et al. 2017, ApJ, 847, 15
Bergemann, M., Hoppe, R., Semenova, E., et al. 2021, MNRAS, 508, 2236

Biémont, E., Palmeri, P., & Quinet, P. 1999, Ap&SS, 269, 635
Blaise, J., Wyart, J.-F., Djerad, M. T., & Ahmed, Z. B. 1984, PhyS, 29, 119
Buder, S., Asplund, M., Duong, L., et al. 2018, MNRAS, 478, 4513
Buder, S., Sharma, S., Kos, J., et al. 2021, MNRAS, 506, 150
Buder, S., Kos, J., Wang, E. X., et al. 2025, PASA, 42, 51
Carlsson, M. 1986, UppOR, 33, 2
Carlsson, M. 1992, in ASP Conf. Ser. 26, Cool Stars, Stellar Systems, and the Sun, ed. M. S. Giampapa & J. A. Bookbinder (San Francisco, CA: ASP), 499
Chen, T.-Y., Shi, J.-R., Beers, T. C., et al. 2021, RAA, 21, 036
Cowan, J. J., Sneden, C., Burles, S., et al. 2002, ApJ, 572, 861
De Silva, G. M., Freeman, K. C., Bland-Hawthorn, J., et al. 2015, MNRAS, 449, 2604
Den Hartog, E. A., Lawler, J. E., Sneden, C., & Cowan, J. J. 2003, ApJS, 148, 543
Doyle, A. P., Davies, G. R., Smalley, B., Chaplin, W. J., & Elsworth, Y. 2014, MNRAS, 444, 3592
Drawin, H. W. 1968, ZPhy, 211, 404
Drawin, H. W. 1969, ZPhy, 225, 470
Ezzeddine, R., Merle, T., & Plez, B. 2016, AN, 337, 850
Ezzeddine, R., Frebel, A., & Plez, B. 2017, ApJ, 847, 142
Ezzeddine, R., Rasmussen, K., Frebel, A., et al. 2020, ApJ, 898, 150
Frebel, A. 2010, AN, 331, 474
Frebel, A. 2018, ARNPS, 68, 237
Frebel, A., Casey, A. R., Jacobson, H. R., & Yu, Q. 2013, ApJ, 769, 57
Gaigalas, G., Kato, D., Rynkun, P., Radžiūtė, L., & Tanaka, M. 2019, ApJS, 240, 29
Gerber, J. M., Magg, E., Plez, B., et al. 2023, A&A, 669, A43
Grevesse, N., Asplund, M., & Sauval, A. J. 2007, SSRv, 130, 105
Guo, Y., Storm, N., Bergemann, M., et al. 2025, A&A, 693, A211
Gustafsson, B., Edvardsson, B., Eriksson, K., et al. 2008, A&A, 486, 951
Hansen, T. T., Holmbeck, E. M., Beers, T. C., et al. 2018, ApJ, 858, 92
Hasselquist, S., Shetrone, M., Cunha, K., et al. 2016, ApJ, 833, 81
Heiter, U., Lind, K., Bergemann, M., et al. 2021, A&A, 645, A106
Holmbeck, E. M., Hansen, T. T., Beers, T. C., et al. 2020, ApJS, 249, 30
Holweger, H., & Mueller, E. A. 1974, SoPh, 39, 19
Hotokezaka, K., Tanaka, M., Kato, D., & Gaigalas, G. 2021, MNRAS, 506, 5863
Hunter, J. D. 2007, CSE, 9, 90
Janicki, C. 1990, CoPhC, 60, 281
Johnson, D. A., & Nelson, P. G. 2017, JPCRD, 46, 013108
Karzas, W. J., & Latter, R. 1961, ApJS, 6, 167
Kupka, F., Piskunov, N., Ryabchikova, T. A., Stempels, H. C., & Weiss, W. W. 1999, A&AS, 138, 119
Lagae, C., Amarsi, A. M., & Lind, K. 2025, A&A, 697, A60
Li, Y., & Ezzeddine, R. 2023, AJ, 165, 145
Lind, K., Asplund, M., Barklem, P. S., & Belyaev, A. K. 2011, A&A, 528, A103
Lind, K., Bergemann, M., & Asplund, M. 2012, MNRAS, 427, 50
Lind, K., & Amarsi, A. M. 2024, ARA&A, 62, 475
Magg, E., Bergemann, M., Serenelli, A., et al. 2022, A&A, 661, A140
Magic, Z., Collet, R., Asplund, M., et al. 2013, A&A, 557, A26
Mardini, M. K., Placco, V. M., Taani, A., Li, H., & Zhao, G. 2019, ApJ, 882, 27
Martell, S. L., Sharma, S., Buder, S., et al. 2017, MNRAS, 465, 3203
Martin, W., Zalubas, R., & Hagan, L. 1978, Atomic Energy Levels—The Rare-Earth Elements (Washington, DC: GPO)
Mashonkina, L., Ryabchikova, T., & Ryabtsev, A. 2005, A&A, 441, 309
Mashonkina, L., Gehren, T., Shi, J.-R., Korn, A. J., & Grupp, F. 2011, A&A, 528, A87
Mashonkina, L., Pakhomov, Y., Sitnova, T., et al. 2023, MNRAS, 524, 3526
Meggers, W. F., Corliss, C. H., & Scribner, B. F. 1975, Tables of Spectral-line Intensities. Part I, II - Arranged by Elements (Washington, DC: GPO)
Menzel, D. H., & Pekeris, C. L. 1935, MNRAS, 96, 77
Merle, T., Thévenin, F., Pichon, B., & Bigot, L. 2011, MNRAS, 418, 863
Nishimura, N., Sawai, H., Takiwaki, T., Yamada, S., & Thielemann, F. K. 2017, ApJL, 836, L21
Placco, V. M., Sneden, C., Roederer, I. U., et al. 2021, RNAAS, 5, 92
Plez, B. 2012, Turbospectrum: Code for Spectral Synthesis, Astrophysics Source Code Library, ascl:1205.004
Pognan, Q., Grumer, J., Jerkstrand, A., & Wanajo, S. 2023, MNRAS, 526, 5220
Reggiani, H., Amarsi, A. M., Lind, K., et al. 2019, A&A, 627, A177
Roederer, I. U., Lawler, J. E., Sneden, C., et al. 2008, ApJ, 675, 723
Roederer, I. U., Sakari, C. M., Placco, V. M., et al. 2018, ApJ, 865, 129
Sakari, C. M., Placco, V. M., Farrell, E. M., et al. 2018, ApJ, 868, 110
Sales-Silva, J. V., Cunha, K., Smith, V. V., et al. 2024, ApJ, 965, 119
Seaton, M. J. 1962a, PPS, 79, 1105
Seaton, M. J. 1962b, in Atomic and Molecular Processes, ed. D. R. Bates (New York: Academic Press), 375
Siegel, D. M., Barnes, J., & Metzger, B. D. 2019, Natur, 569, 241
Sneden, C., Cowan, J. J., & Gallino, R. 2008, ARA&A, 46, 241
Storm, N., & Bergemann, M. 2023, MNRAS, 525, 3718
Strassmeier, K. G., Ilyin, I., & Steffen, M. 2018, A&A, 612, A44
Travis, L. D., & Matsushima, S. 1968, ApJ, 154, 689
Watson, D., Hansen, C. J., Selsing, J., et al. 2019, Natur, 574, 497
Wenger, M., Ochsenbein, F., Egret, D., et al. 2000, A&AS, 143, 9
Westin, J., Sneden, C., Gustafsson, B., & Cowan, J. J. 2000, ApJ, 530, 783
Xu, H. L., Svanberg, S., Cowan, R. D., et al. 2003, MNRAS, 346, 433